

Numerical Simulations of Compressible Mixing Layers with High-order ENO-schemes

Tilo Lumpp

▶ **To cite this version:**

Tilo Lumpp. Numerical Simulations of Compressible Mixing Layers with High-order ENO-schemes. RR-2379, INRIA. 1994. inria-00074298

HAL Id: inria-00074298
https://inria.hal.science/inria-00074298

Submitted on 24 May 2006

HAL is a multi-disciplinary open access archive for the deposit and dissemination of scientific research documents, whether they are published or not. The documents may come from teaching and research institutions in France or abroad, or from public or private research centers.

L'archive ouverte pluridisciplinaire **HAL**, est destinée au dépôt et à la diffusion de documents scientifiques de niveau recherche, publiés ou non, émanant des établissements d'enseignement et de recherche français ou étrangers, des laboratoires publics ou privés.



INSTITUT NATIONAL DE RECHERCHE EN INFORMATIQUE ET EN AUTOMATIQUE

Numerical Simulations of Compressible Mixing Layers with High-order ENO-schemes

Tilo LUMPP

N° 2379
Octobre 1994

PROGRAMME 6



Les rapports de recherche de l'INRIA
sont disponibles en format postscript sous
ftp.inria.fr (192.93.2.54)

si vous n'avez pas d'accès ftp
la forme papier peut être commandée par mail :
e-mail : dif.gesdif@inria.fr
(n'oubliez pas de mentionner votre adresse postale).

par courrier :
Centre de Diffusion
INRIA
BP 105 - 78153 Le Chesnay Cedex (FRANCE)

INRIA research reports
are available in postscript format
ftp.inria.fr (192.93.2.54)

if you haven't access by ftp
we recommend ordering them by e-mail :
e-mail : dif.gesdif@inria.fr
(don't forget to mention your postal address).

by mail :
Centre de Diffusion
INRIA
BP 105 - 78153 Le Chesnay Cedex (FRANCE)



Numerical Simulations of Compressible Mixing Layers with High-order ENO-schemes

Tilo LUMPP *

Programme 6 — Calcul scientifique, modélisation et logiciel numérique
Projet Sinus

Rapport de recherche n ° 2379 — October 1994 —

Abstract: In this report some experiences that were made with high-order finite-volume ENO-schemes are reported. In a first section the most important parts of the numerical method, the reconstruction and the choice of the stencil are presented, at the example of the linear advection equation. The extension of the ENO-algorithm to the Euler and the Navier-Stokes equations is shown. The stability-properties and the precision of ENO-schemes are discussed. In a second section the presented method is applied to the full Navier-Stokes equations. The chosen test-case concerns a compressible mixing-layer at transonic and subsonic Mach-numbers. Computations with third-order ENO show that the numerical method captures shocks and contact discontinuities well. Fourth-order ENO-computations make difficulties on fine grids.

(Résumé : tsvp)

*INRIA Sophia-Antipolis, B. P. 93, 2004, route des Lucioles, 06902 Sophia-Antipolis/ France

Unité de recherche INRIA Sophia-Antipolis
2004 route des Lucioles, BP 93, 06902 SOPHIA-ANTIPOLIS Cedex (France)
Téléphone : (33) 93 65 77 77 – Télécopie : (33) 93 65 77 65

Simulations numériques de couches de mélanges compressibles avec des schémas d'ordre élevés du type ENO

Résumé : Dans ce rapport, quelques expériences qui ont été faites avec des schéma volumes finis d'ordre élevé du type ENO sont rapportés. Dans une premiére partie, les parties centrales de la méthode numérique, la reconstruction et le choix du stencil, sont présentées à l'aide de l'équation d'advection. L'extension de l'algorithme aux équations d'Euler et les équations de Navier-Stokes est montrée. Les propriétés de stabilité et la précision de la méthode sont discutés. Dans une deuxième partie, l'algorithme est appliqué aux équations de Navier-Stokes. Le cas test choisi est constitué d'une couche de mélange à des nombres de Mach transoniques et subsoniques. La méthode numérique montre des bonnes propriétés de capturer des shocks et des discontinuités de contacte lorsque des schémas précises au troisième sont utilisés. Des calculs avec des schémas ENO précises au quatrième ordre font des problèmes lorsque les maillages fins sont utilisés.

Contents

1 Introduction **3**

2 The Mixing-layer **3**
2.1 The Compressible Navier-Stokes-equations 3
2.2 Some results from linear analysis of stability and direct numerical simulation 5

3 Numerical method **10**
3.1 Finite-Volume discretisation 10
3.2 Reconstruction with a rectangular stencil 13
3.3 Evaluation of the fluxes 17
3.4 Artificial viscosity 18
3.5 Computation of the viscous fluxes 20
3.6 Time-integration 22
3.7 Stability properties of ENO-schemes 24
3.8 On the precision of ENO-schemes 24

4 Results **25**
4.1 Physical problem 25
4.2 Tools for analysing the flow-field 28
4.3 Simulations at transonic Mach numbers with one vortex . . . 29
4.4 Simulations at transonic Mach numbers with two vortices . . . 33
4.5 Simulations at subsonic Mach numbers with two vortices . . . 39
4.6 Simulations with 4th-order ENO-schemes 44

5 Conclusion **47**

1 Introduction

Turbulence and the transition to it are now investigated for more than one century. Pioneer works have been done by e. g. Helmholtz [10]. Until now, there are neither rigorous descriptions of turbulence itself nor of the transition to it. The - very simple - picture that one has of transition is, that an instable flow is subject of small perturbations. These perturbations are amplified in space and time, vortices come up and interact eventually. At the moment, there are three ways to investigate transition to turbulence: Experiments, theory (especially analysis of stability) and numerical simulations.

In a first section a very brief overview of the existing experiences will be given. Especially, several authors, who have observed an enormous influence of the numerical methodology and the precision of the solution on the results will be cited. This is the motiviation why in this study high-order ENO-schemes will be applied to shear-flow.

In the second section, the ENO-scheme used in this study will be briefly presented, together with some already existing experiences that were made with these new schemes. In the last two sections results will be shown and commented.

2 The Mixing-layer

Before giving a short survey of the experiences that were already made in the field of numerical simulation of transonic shear-layer, the compressible Navier-Stokes-equations will be given.

2.1 The Compressible Navier-Stokes-equations

The physical problem is a two-dimensional temporally developping mixing layer. The domain of calculation Ω is a rectangle of length L_x in horizontal direction and $2L_y$ in vertical direction, i. e.

$$0 \leq x \leq L_x \qquad -L_y \leq y \leq L_y \tag{1}$$

The Navier-Stokes-equations write in dimensionless form:

$$\frac{\partial \vec{q}}{\partial t} + \frac{\partial \vec{F}}{\partial x} + \frac{\partial \vec{G}}{\partial y} = \frac{1}{Re}\frac{\partial \vec{R}}{\partial x} + \frac{1}{Re}\frac{\partial \vec{S}}{\partial y} \tag{2}$$

The primitive variables of the fluid are density ρ, vector of velocities $\vec{u} = [u, v]^T$, pressure p, and temperature T. The vector of conservative variables is

$$\vec{q} = \begin{bmatrix} \rho \\ \rho u \\ \rho v \\ e \end{bmatrix} \qquad \text{with } e = \frac{p}{\gamma - 1} + \frac{1}{2}\rho(u^2 + v^2) \tag{3}$$

So e is the total energy of the fluid, $\gamma = \frac{c_p}{c_v} = 1.4$ is the ratio of the specific heats. The Euler fluxes in horizontal direction x and vertical direction y are

$$\vec{F} = \begin{bmatrix} \rho u \\ \rho u^2 + p \\ \rho uv \\ u(e+p) \end{bmatrix} \qquad \vec{G} = \begin{bmatrix} \rho v \\ \rho uv \\ \rho v^2 + p \\ v(e+p) \end{bmatrix} \tag{4}$$

The viscous fluxes are

$$\vec{R} = \begin{bmatrix} 0 \\ \tau_{xx} \\ \tau_{xy} \\ u\tau_{xx} + v\tau_{xy} + \frac{1}{PrMa^2(\gamma-1)}\frac{\partial T}{\partial x} \end{bmatrix} \vec{S} = \begin{bmatrix} 0 \\ \tau_{xy} \\ \tau_{yy} \\ u\tau_{xy} + v\tau_{yy} + \frac{1}{PrMa^2(\gamma-1)}\frac{\partial T}{\partial y} \end{bmatrix} \tag{5}$$

respectively.

The shear stresses are $\tau_{xx} = \frac{2}{3}\mu(2\frac{\partial u}{\partial x} - \frac{\partial v}{\partial y})$, $\tau_{xy} = \mu(\frac{\partial u}{\partial y} + \frac{\partial v}{\partial x})$, $\tau_{yy} = \frac{2}{3}\mu(2\frac{\partial v}{\partial y} - \frac{\partial u}{\partial x})$. In this study, the viscosity μ and the thermal conductiviy k are assumed to be a constant $(= 1)$.

In the above non-dimensionalized equations, the quantities ρ_∞, $2u_\infty$, T_∞, μ and k have been used, where the index ∞ denotes, that a quantity is taken at free-stream conditions. The characteristic length of the problem is δ_i, the thickness of the shear layer at the beginning of the computation.

The dimensionless numbers (Reynolds number Re, Prandtl number Pr, Mach number Ma) are defined by:

$$Re = \frac{2u_\infty \cdot \delta_i \cdot \rho_\infty}{\mu} \qquad Pr = \frac{c_p \mu}{k} \qquad Ma = \frac{2u_\infty}{\sqrt{\gamma R T_\infty}} \tag{6}$$

It is easily seen, that the reference Mach number defined here is twice the convective Mach number Ma_c. To complete the set of governing equations, it is necessary to give the equation of state in dimensionless form:

$$p = \frac{1}{\gamma Ma^2} \rho T \tag{7}$$

2.2 Some results from linear analysis of stability and direct numerical simulation

One of the most-investigated types of unstable flow is the mixing layer. Several authors have investigated this issue either from the point of view of linear analysis of stability or from the point of direct numerical simulation. A short review of their results will now be given.

One often cited work is the work of Michalke [15]. He investigates the stability-properties of a two-dimensional, incompressible and non-viscous shear-layer. He takes a hyperbolic-tangent velocity-profile as basis profile U, to which he adds a small sinusoidal perturbation u'.

$$U = \frac{1}{2}[1 + \tanh(y)] \tag{8}$$

$$u' = \Phi(y) \cdot \exp[i\alpha(x - c \cdot t)] \tag{9}$$

α indicates the wave-number of the perturbation, x the spatial direction and c is a complex number ($c = c_r + ic_i$). The real part c_r is the phase velocity and the imagimary part c_i measures the amplification rate. Inserting eq. 8 and 9 into the Euler-equations of incompressible flow and linearisation in u' gives the Rayleigh-stability equation:

$$(U - c) \cdot (\Phi'' - \alpha^2 \Phi) - U'' = 0. \tag{10}$$

Together with the boundary-conditions $\Phi(-\infty) = \Phi(\infty) = 0$, Michalke solved the stability-equation numerically. He found the most amplified wavelength to be $\alpha = 0.4446$ and its amplification rate to be $\alpha \cdot c_i^{max} = 0.0949$.

Blumen [4] extended the work of Michalke to compressible flow. He observes, that the wavelength λ of the most amplified mode increases with the Mach number. He also reports, that the amplification rate $\alpha \cdot c_i$ decreases with increasing Mach numbers.

Sandham and Reynolds [18] studied the stability-properties of compressible, inviscid and three-dimensional shear-layers. They investigated temporal as well as spatial evolution of a perturbed shear-layer. Their basic velocity profile is $U = \tanh(2y)$ and not $U = \tanh(y)$ as before. Here only the results of temporal evolution will be cited briefly. They confirmed the results of Michalke and Blumen (Fig. 1). Furthermore they observe, that for three-dimensional flow oblique modes become dominating (Fig. 2).

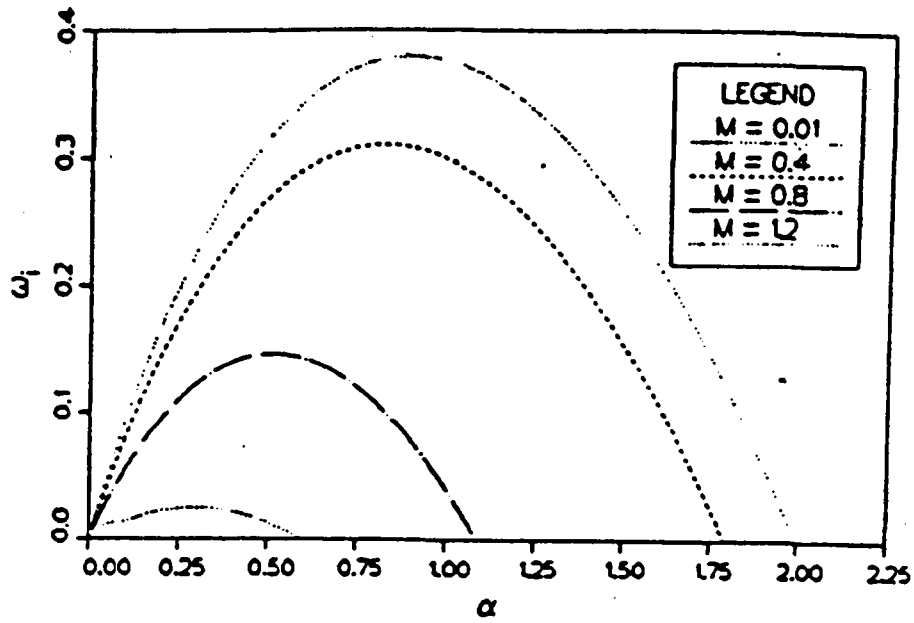


Figure 1: Wavenumber and amplification-rates for hyperbolic-tangent flow (from [18])

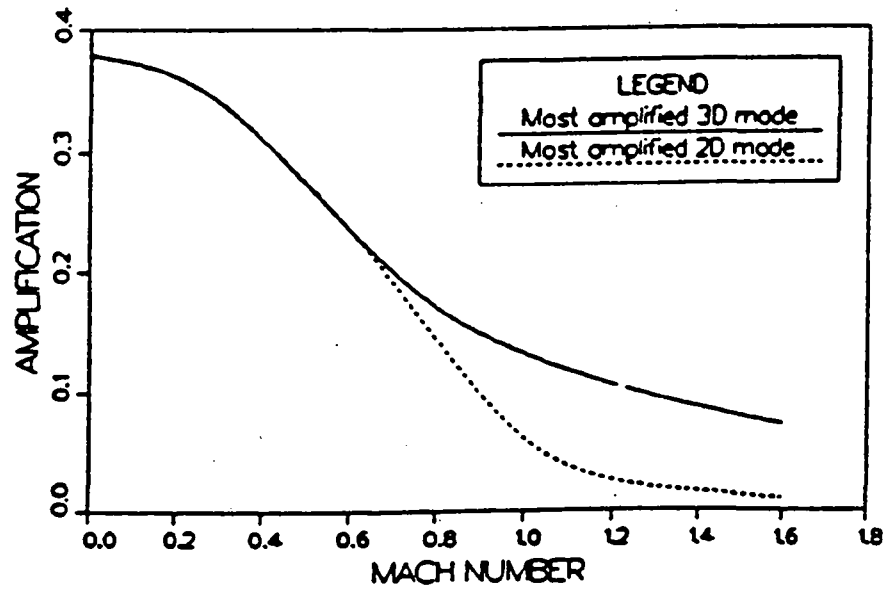


Figure 2: Amplification-rates of 2d- and 3d-perturbations for hyperbolic-tangent flow from ([18])

The results from linear stability analysis are often used for direct numerical simulations. One often-investigated configuration is a box of length L_x and width L_y. The basic flow is hyperbolic-tangent with small sinusoidal perturbation. The full Navier-Stokes equations are solved numerically for this problem.

The choice of the numerical methodology is of great importance for this subject, where tiny effects can become, due to amplification, very important. Different concurrent numerical methods were applied to shear-flow, namely spectral-methods, finite-volume or finite-difference methods and Padé-schemes.

The choice of spectral methods in this issue is obvious. It is well-known, that spectral-methods delivier high-order spatial approximations and do not need explicit numerical viscosity for stable algortihms. Normally, for time-dicretization second- or third-order accurate schemes are used. So if numerical errors appear, they are normally attributed to time-discretization. So there is some hope that especially at the beginning of the computation, when small perturbations are amplified, trustful results are given and a benchmarking is provided. But spectral methods fail if shocks appear. On the contrary finite-volume or finite-difference schemes allow to treat shocks, but it is necessary to introduce numerical dissipation terms, that can become dominant, especially if small structures are investigated. Most finite-volume or finite-difference schemes are only first- or second-order accurate.

There exist several numerical simulations that were carried out with spectral-methods. In a second part of their study, Sandham and Reynolds [18] apply a spectral-like scheme in x-direction and a high-order Padé scheme in y-direction. L_x is choosen to be λ_{max} where λ_{max} is the most amplified wavelength according to linear analysis of stability. The Mach number Ma, taken at freestream-conditions, is $Ma = 0.6$. One vortex should be created, what is indeed observed. The numerical amplification-rates correspond well to the theoretical predictions.

Guillard et al. [7] investigated compressible shear-flow at transonic Mach numbers with an adaptive spectral-method before appearance of shocks. The test-case is basically the same as above, but the Mach number (defined as before) is increased to $Ma = 0.8$ and length and width of the computational

domain are adapted to the corresponding most amplified wavelength. In [12] the results obtained with the algorithm of Guillard et al. are compared with those of a 2nd order MUSCL method at different Mach numbers for deterministic and random perturbations. In all cases a good agreement is obtained if the initial condition consists of perturbations with sufficiently high amplitudes.

In a second study, carried out with H. C. Yee, Sandham [19] investigates the transonic shear-layer with second-order TVD-schemes. Their conclusion is that the limiters, inherent to most TVD-schemes influence, enormously the results. The most striking result is that for the integral quantity vorticity thickness (what is a measure fort the growth of the shear-layer) differences of up to 50 % are observed depending on the TVD-viscosity that was used.

Atkins [2] continues to exploit the results of linear analysis of stability. He uses the same test-case as before, but a Mach number of $Ma = 0.5$ and uses $L_x = 2 \cdot \lambda_{max}$ (λ_{max} is the most amplified wavelength at $Ma = 0.5$). He only exites the mode $\lambda = \lambda_{max}$, all other distrubances vanish, including the interaction forcing mode. So two vortices should emerge and eventually interact. Atkins observes indeed the creation of two vortices. With an analysis of the time-evolution of the kinetic energy-spectra, he shows that the mode that forces the vortices to interact is amplified in a non-physical way due to the numerical dissipation.
Similar experiences have been made in [12] at $Ma = 0.8$.

The results of the numerical experiences can be summarized as:

- Linear analysis of stability is valuable tool for analysing shear-flow at subsonic as well as at transonic Mach numbers.
- For subsonic shear-layers and determinitsic perturbations with sufficiently high amplitudes the results of the different numerical schemes (Padé, spectral, MUSCL) do not differ very much and coincide well with the predictions of linear analysis of stability.
- If the amplitudes of the perturbations tend towards zero unphysical amplification-rates are observed with finite-volume schemes. The reason for this is numerical dissipation inherent in most finite-volume

schemes

- If shocks appear severe problemes come up as the TVD-viscosity influences enormously the results.

This shows a definite necessity for the development of finite-volume schemes that are

- less dissipative as conventional TVD-schemes
- and can handle shocks without limitation

The most promising conception of less dissipative schemes that can handle shocks is the ENO-conception of Harten [9], Shu [20] and their co-workers. The goal of this study is to apply a high-order ENO-scheme that can handle shocks and should be less dissipative than conventional MUSCL-schemes. The results will be compared with the predictions of linear analysis of stability and MUSCL- and spectral computations. The effects of numerical dissipation will be discussed.

3 Numerical method

3.1 Finite-Volume discretisation

Now, the two principal points of the high-order ENO-scheme, the reconstruction and the choice of the stencil, will be given. A detailed description of these schemes can be found in [5], [8] and [13].

Let us look at the two-dimensional advection-equation

$$\frac{\partial u}{\partial t} + \frac{\partial f(u)}{\partial x} + \frac{\partial g(u)}{\partial y} = 0 \tag{11}$$

with boundary-conditions (to be specified later) and initial conditions $u(x, y, 0)$. It is well known, that the solution of eq. (11) can develop discontinuities, even for smooth initial conditions. In [5] a numerical procedure for high-order approximations of smooth solutions of (11) is presented.

For the sake of simplicity, use a cartesian grid with gridpoints x_i, y_j. A computational cell is given by (see Fig. 3)

$$C_{i,j} = [x_i - \frac{dx_{i-1}}{2}, x_i + \frac{dx_i}{2}] \times [y_j - \frac{dy_{j-1}}{2}, y_j + \frac{dy_j}{2}] \tag{12}$$

$$dx_i = (x_{i+1} - x_i) \qquad dy_j = (y_{j+1} - y_j) \tag{13}$$

The cell-average of u over the cell $C_{i,j}$ is:

$$\overline{u}_{i,j}(t) = \frac{1}{\Delta x_i \cdot \Delta y_j} \int_{x_i - \frac{dx_{i-1}}{2}}^{x_i + \frac{dx_i}{2}} \int_{y_j - \frac{dy_{j-1}}{2}}^{y_j + \frac{dy_j}{2}} u(\xi, \eta, t) d\xi d\eta \tag{14}$$

with $\Delta x_i = \frac{1}{2}(dx_{i-1} + dx_i)$ and an analogous definition for Δy_j. This cell-average satisfies, in a semi-discrete notation

$$\frac{d\overline{u}_{i,j}}{dt} = -\frac{1}{\Delta x_i \cdot \Delta y_j} \cdot \{\hat{f}_{i+\frac{1}{2},j}(t) - \hat{f}_{i-\frac{1}{2},j}(t) + \hat{g}_{i,j+\frac{1}{2}}(t) - \hat{g}_{i,j-\frac{1}{2}}(t)\} \tag{15}$$

even if weak solutions appear. The (exact) fluxes $\hat{f}_{i+\frac{1}{2},j}(t), \hat{g}_{i,j+\frac{1}{2}}(t) \cdots$ have the form

$$\hat{f}_{i+\frac{1}{2},j}(t) = \int_{y_j - \frac{dy_{j-1}}{2}}^{y_j + \frac{dy_j}{2}} f(u(x_i + \frac{dx_i}{2}, \eta, t)) d\eta \tag{16}$$

$$\hat{g}_{i,j+\frac{1}{2}}(t) = \int_{x_i - \frac{dx_{i-1}}{2}}^{x_i + \frac{dx_i}{2}} g(u(\xi, y_j + \frac{dy_j}{2}, t)) d\xi \tag{17}$$

Eq. (15) suggests a "method of lines" approach in time. For every $t = const$ line eq. (15) can be written as

$$\frac{d\overline{u_{i,j}}(t^n)}{dt} = \mathcal{L}(\overline{u}_{i,j}(t^n)) \tag{18}$$

so time-integration and spatial derivation can be treated separately.

Only the most important steps (reconstruction and choice of the stencil) will be explained in the next section.

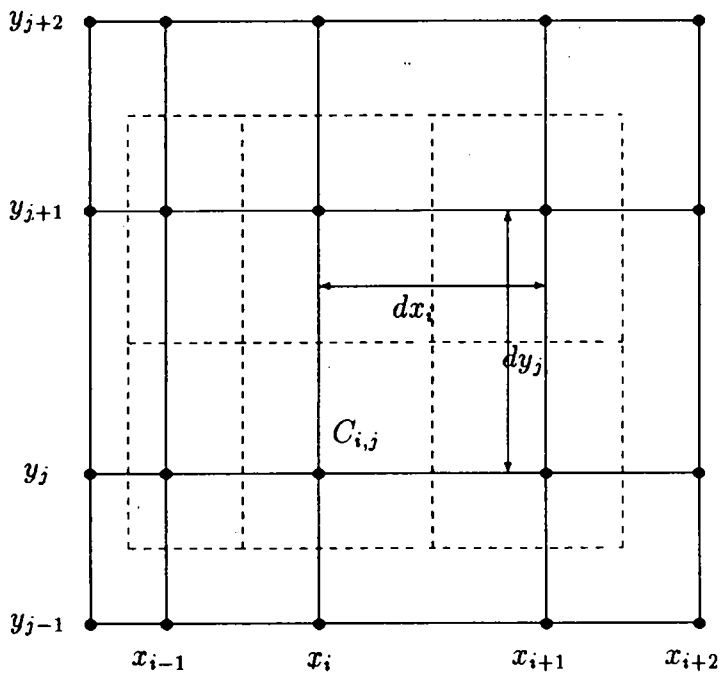


Figure 3: Computational grid and cells

3.2 Reconstruction with a rectangular stencil

In this section a reconstruction procedure for a two-dimensional function on a structured grid will be given. The extension of ENO-schemes to unstructured grids is not evident and will not be shown here. The reader is referred to [1]. This reconstruction procedure, uses two one-dimensional interpolations. In a first step the mean-values of u e. g. in y-direction are computed. These mean-values are the starting points for the reconstruction in y-direction. This reconstruction procedure was introduced by Casper and Atkins [5].
Start with the definition of the mean-value of u over the cell $C_{k,l}$

$$\overline{u}_{k,l} = \frac{1}{\Delta x_k \cdot \Delta y_l} \int_{x_k - \frac{dx_{k-1}}{2}}^{x_k + \frac{dx_k}{2}} \int_{y_l - \frac{dy_{l-1}}{2}}^{y_l + \frac{dy_l}{2}} u(\xi, \eta) d\xi d\eta \tag{19}$$

(with dx_k and dy_l as in eq. (13), $\Delta x_k = \frac{1}{2}(dx_{k-1} + dx_k)$.)
Define now a primitive function $\overline{U_l(x)}$

$$\overline{U_l(x)} = \int^x \frac{1}{\Delta y_l} \int_{y_l - \frac{dy_{l-1}}{2}}^{y_l + \frac{dy_l}{2}} u(\xi, \eta) d\xi d\eta \tag{20}$$

The exact values of this primitive function are known along the lines

$$x_{k+\frac{1}{2}} = x_k + \frac{1}{2} dx_k \qquad\qquad y_l - \frac{dy_{l-1}}{2}, .., y_l + \frac{dy_l}{2} \tag{21}$$

and the values of the primitive function are obtained from (19)

$$\sum_{k=i_0}^{i} \Delta x_k \cdot \overline{u_{k,l}} = \int_{x_{i_0}}^{x_{i+\frac{1}{2}}} \frac{1}{\Delta y_l} \int_{y_l - \frac{dy_{l-1}}{2}}^{y_l + \frac{dy_l}{2}} u(\xi, \eta) d\xi d\eta \tag{22}$$

With Newton's divided difference interpolation formula [11] a polynomial $P_l^r(x)$, that approximates $\overline{U_l}(x)$ to $(r+1)$-th order can be found. One has

$$P_l^r(x) = \overline{U_l}(x) + O(\Delta x)^{r+1} \tag{23}$$

The derivatives of P_l^r and $\overline{U_l(x)}$ satisfy the following relations:

$$\frac{d}{dx}\overline{U_l(x)} = \frac{d}{dx} \int_{x_0}^{x_{i+\frac{1}{2}}} \frac{1}{\Delta y_l} \int_{y_l - \frac{1}{2}dy_{l-1}}^{y_l + \frac{1}{2}dy_l} u(\xi, \eta) d\xi d\eta = \frac{1}{\Delta y_l} \int_{y_l - \frac{1}{2}dy_{l-1}}^{y_l + \frac{1}{2}dy_l} u(x_{i+\frac{1}{2}}, \eta) d\eta \equiv \overline{u_l}(x) \tag{24}$$

$$p_l^r(x) \equiv \frac{d}{dx} P_l^r(x) = \frac{d}{dx}(\overline{U_l}(x) + O(\Delta x)^{r+1}) = \overline{u_l}(x) + O(\Delta x)^r \tag{25}$$

Each polynomial of the set $\{p_l^r, l = 0, jmax\}$ is a high-order approximation of the corresponding function of the set $\{\overline{u_l}, l = 0, jmax\}$. For fixed x the polynomials of the set $\{p_l^r, l = 0, jmax\}$ are one-dimensional cell-averages in y-direction on the interval $[y_{j-\frac{1}{2}}, y_{j+\frac{1}{2}}]$ of a piecewise smooth function $p(x, y)$. One wants to find a pointwise high-order reconstruction of p in y-direction. Therefore define an associated primitive function by:

$$\Pi(x, y) = \int^y p(x, \eta) d\eta \tag{26}$$

The exact values of Π are known on the half-points of the grid, they are

$$\sum_{l=j_0}^{j} p_l^r(x) \Delta y_l = \int_{y_{j_0}}^{y} p(x, \eta) d\eta \tag{27}$$

The new primitive function $\Pi(x, y)$ can be approximated by a new interpolation polynomial $Q^r(x, y)$, which satisfies

$$Q^r(x, y) = \Pi(x, y) + O(\Delta y)^{r+1} \tag{28}$$

The derivative of Π gives the desired function $p(x, y)$. The derivatives of $\Pi(x, y)$ and $Q^r(x, y)$ satisfy:

$$\frac{d}{dy}\Pi(x, y) = \frac{d}{dy}\int_{y_0}^{y} p(x, \eta) d\eta = u(x, y) \tag{29}$$

$$\frac{d}{dy}Q^r(x, y) = p(x, y) + O(\Delta y)^r \tag{30}$$

Applying the error- and reconstruction-relations above shows that $\frac{d}{dx}Q^r(x, y)$ in eq. (30) is a r-th order reconstruction of $u(x, y)$.

Note, that the explicit computation of the primitive functions $\overline{U_l}(x)$ and $\Pi(x, y)$ is not necessary, since we are only interested in their derivatives $\overline{u_l}(x)$ and $p(x, y)$. Consider e. g. the interpolation polynomial $P_l^2(x)$. One possible stencil, that can be used for reconstruction is $\{x_{i-\frac{1}{2}}, x_{i+\frac{1}{2}}, x_{i+\frac{3}{2}}\}$. P_l^2 is then

$$P_l^2(x) = \overline{U_l}[x_{i-\frac{1}{2}}]\cdot\omega_0(x)+\overline{U_l}[x_{i-\frac{1}{2}}x_{i+\frac{1}{2}}]\cdot\omega_1(x)+\overline{U_l}[x_{i-\frac{1}{2}}x_{i+\frac{1}{2}}x_{i+\frac{3}{2}}]\cdot\omega_2(x) \quad (31)$$

The derivative of $P_2^r(x)$ is

$$\frac{d}{dx}P_2^r = \overline{U_l}[x_{i-\frac{1}{2}}]\cdot\omega_0'(x)+\overline{U_l}[x_{i-\frac{1}{2}},x_{i+\frac{1}{2}}]\cdot\omega_1'(x)+\overline{U_l}[x_{i-\frac{1}{2}}x_{i+\frac{1}{2}}x_{i+\frac{3}{2}}]\cdot\omega_2'(x) \quad (32)$$

The coefficients $\overline{U_l}[x_{i-\frac{1}{2}}x_{i+\frac{1}{2}}]$ can be obtained immediately from:

$$\Delta x_i\overline{u_{i,j}} = \overline{U_l}(x_{i+\frac{1}{2}}) - \overline{U_l}(x_{i-\frac{1}{2}}) \quad (33)$$

$$\Rightarrow \overline{u_i} = \frac{\overline{U_l}(x_{i+\frac{1}{2}}) - \overline{U_l}(x_{i-\frac{1}{2}})}{\Delta x_i} = \overline{U_l}[x_{i-\frac{1}{2}}x_{i+\frac{1}{2}}] \quad (34)$$

and the polynomials $\omega(x)$ are given by:

$$\begin{aligned}\omega_0(x) &= 1\\ \omega_n(x) &= \omega_{n-1}(x - x_{i-\frac{1}{2}+n-1}) \qquad n \geq 1\end{aligned} \quad (35)$$

Their derivatives are computed recursively by:

$$\omega_n'(x) = \frac{\partial}{\partial x}[\omega_{n-1}\cdot(x-x_{i-\frac{1}{2}+n})] = \begin{cases} 0 & \text{if } n = 0\\ 1 & \text{if } n = 1\\ \omega_{n-1}'\cdot(x - x_{i-\frac{1}{2}+n-1}) + \omega_{n-1} & \text{if } n \geq 2\end{cases} \quad (36)$$

Choice of the stencil

Now, the choice of the stencil, i. e. the set of the cells, used for the reconstruction is going to be described. Harten et al. [8] pointed out that an adaptive stencil must be used in order to stabilize the algorithm. It is selected according to the smoothness of the function and its derivatives. The criterion is, that in the vicinity of the cell $C_{k,l}$ the part of the function must be used where the function and its derivatives are smoothest. The information about the smoothness of u can be extracted from the table of the divided differences. Especially, the divided differences have the following properties [8], [9]:

- If u is C_∞ in $[x_i, x_{i+k}]$ then

$$u[x_i \cdots x_{i+k}] = \frac{1}{k!}\frac{\partial^k}{\partial x^k}u(\xi_{i,k}), \qquad x_i \leq \xi_{i,k} \leq x_{i+k} \tag{37}$$

- If u exhibits a discontinuity in the p-th derivative within $[x_i, x_{i+k}]$, then for $0 \leq p \leq k$

$$u[x_i \cdots x_{i+k}] = O(\Delta x)^{-k+p}[w^{(p)}] \tag{38}$$

$[w^{(p)}]$ denotes the jump in the p-th derivative. Eq. (37) and (38) allow to estimate the smoothness of u and its derivatives. This can be seen as follows: suppose that u is smooth in (x_{i_1}, x_{i_1+k}) but discontinous in (x_{i_2}, x_{i_2+k}) then $|u[x_{i_1} \cdots x_{i_1+k}]| < |u[x_{i_2} \cdots x_{i_2+k}]|$ for Δx sufficiently small. If u or one of its derivatives has a jump, this will be reflected in the corresponding divided difference. This shows that the task of choosing the smoothest part of u is closely related to the task of finding the set of points where the absolute values of the divided differences are smoothest.

Since for the reconstruction procedure two one-dimensional interpolations are used, it is sufficient to find the "minimising" stencil for each direction. The choice of the "minimising" stencil for the interpolation in x-direction is now descripted. The same procedure is used for the choice of the stencil in y-direction.
The divided differences can be computed recursively from (see [11]):

$$\overline{U}_l[x_{i-\frac{1}{2}}] = \overline{U}_l(x_{i-\frac{1}{2}}) \tag{39}$$

$$\overline{U}_l[x_{i-\frac{1}{2}}x_{i+\frac{1}{2}}] = \frac{\overline{U}_l[x_{i-\frac{1}{2}}] - \overline{U}_l[x_{i+\frac{1}{2}}]}{x_{i+\frac{1}{2}} - x_{i-\frac{1}{2}}} \tag{40}$$

$$\overline{U}_l[x_{i-\frac{1}{2}}x_{i+\frac{1}{2}}x_{i+\frac{3}{2}}] = \frac{\overline{U}_l[x_{i+\frac{1}{2}}x_{i+\frac{3}{2}}] - \overline{U}_l[x_{i-\frac{1}{2}}x_{i+\frac{1}{2}}]}{x_{i+\frac{3}{2}} - x_{i-\frac{1}{2}}} \tag{41}$$

$$\vdots$$

Denote the leftmost point of the stencil by $irec_l(i)$, where the index i indicates the x-coordinate and l indicates the y-coordinate of the cell within u is to be reconstructed. Start with $irec_l(i) = i$. To obtain the next-higher order one

can add the two cells x_{i-1} and x_{i+1}. The choice, which one is to be used will depend on the absolute values of the corresponding devided differences

$$|\overline{U}_l[x_{i-\frac{3}{2}}x_{i-\frac{1}{2}}x_{i+\frac{1}{2}}]| \text{ and } |\overline{U}_l[x_{i-\frac{1}{2}}x_{i+\frac{1}{2}}x_{i+\frac{3}{2}}]| \tag{42}$$

Apply now:

if $|\overline{U}_l[x_{i-\frac{3}{2}}x_{i-\frac{1}{2}}x_{i+\frac{1}{2}}]| < |\overline{U}_l[x_{i-\frac{1}{2}}x_{i+\frac{1}{2}}x_{i+\frac{3}{2}}]|$ then
$irec_l(i) = irec_l(i) - 1$
endif

The stencil is shifted to the left, if the absolute value of $|\overline{U}_l[x_{i-\frac{3}{2}}x_{i-\frac{1}{2}}x_{i+\frac{1}{2}}]|$ is smaller than $|\overline{U}_l[x_{i-\frac{1}{2}}x_{i+\frac{1}{2}}x_{i+\frac{3}{2}}]|$. If not the point $x_{i+\frac{1}{2}}$ is added. Repeat this procedure until the stencil is determined. Visibly the same procedure can be applied for the reconstruction in y-direction.

3.3 Evaluation of the fluxes

The fluxes to be approximated numerically are (e. g. in x-direction) from eq. (16)

$$\hat{f}_{i+\frac{1}{2},j}(t) = \int_{y_j-\frac{\Delta y_{j-1}}{2}}^{y_j+\frac{\Delta y_j}{2}} f(u(x_i + \frac{\Delta x_i}{2}, \eta, t))d\eta \tag{43}$$

In order to stabilize the numerical scheme, it is necessary to introduce a certain amount of artificial viscosity. It is supposed that the numerical fluxes satisfy

$$\hat{f} = \overline{f} + O(\Delta x^r, \Delta y^r) \tag{44}$$

where $\overline{f}$ is the numerical flux defined in the next section. So integral (16) becomes

$$\int_{y_j-\frac{\Delta y_{j-1}}{2}}^{y_j+\frac{\Delta y_j}{2}} \hat{f}(x,\eta)d\eta = \int_{y_j-\frac{\Delta y_{j-1}}{2}}^{y_j+\frac{\Delta y_j}{2}} \overline{f}(u(x,\eta))d\eta + O(\Delta x)^{r+1} \tag{45}$$

This integral is computed numerically with a Gauß quadrature formula. It is well-known that (see [11])

$$I \equiv \int_a^b f(\eta)d\eta = \sum_{j=1}^{n} \alpha_j f(\eta_j) + E_n\{f\} \tag{46}$$

is an approximation of order $2n$ to I if:

1. n points $\eta_j \in [a,b]$ are used for the numerical integration.
2. an interpolation formula is used for the computation of the discrete values $f(\eta_j)$.
3. f has $2n$ continuous derivatives.

Then the error $E_n\{f\}$ is found to be

$$E_n f = \frac{f^{(2n)}(\eta)}{(2n!)} \int_a^b P_n^2(\eta) d\eta \tag{47}$$

with $\eta_j \in (a,b)$ and $P_n(\eta) = (\eta - \eta_0) \cdot (\eta - \eta_1) \cdots (\eta - \eta_{n-1})$, where the η_l are the points used for the interpolation formula. The coefficients α_i of eq. (46) can be computed by

$$\alpha_i = \frac{1}{[P_n'(\eta_j)]^2} \int_a^b \frac{P_n^2(\eta)}{(\eta - \eta_j)^2} d\eta \tag{48}$$

The set of points η_j that are used for the Gauß quadrature can be choosen arbitrarily within (a,b). But for certain points, the coefficients α_j become very simple. For an equidistant mesh ($\Delta y_j = \Delta y_{j-1} \forall j$) choose e. g.

$$y_1 = \frac{a+b}{2} - \frac{1}{\sqrt{3}}(\frac{b-a}{2}) = \cdots = y_j - \frac{1}{\sqrt{3}}\frac{\Delta y_j}{2} \tag{49}$$

$$y_2 = \frac{a+b}{2} + \frac{1}{\sqrt{3}}(\frac{b-a}{2}) = \cdots = y_j + \frac{1}{\sqrt{3}}\frac{\Delta y_j}{2} \tag{50}$$

The corresponding coefficients α_1 and α_2 become

$$\alpha_1 = \frac{1}{2}\Delta y_j \qquad\qquad \alpha_2 = \frac{1}{2}\Delta y_j \tag{51}$$

For sufficiently smooth functions I is approximated to 4^{th} order, if the $f(\eta_i)$ are approximated to 4^{th} order.

3.4 Artificial viscosity

To stabilize the algorithm, artificial viscosity has to be introduced. In this work, a Roe-type numerical viscosity is used [16]. For the simple advection

equation the numerical fluxes in x-direction at $x = x_i + \frac{1}{2}\Delta x_i$ are:

$$\overline{f}^n(x_{i+\frac{1}{2}}, y_j) = \frac{1}{2}\{f(u^+(x_i, y_j)) + f(u^-(x_{i+1}, y_j)) - \|a(u_i^+, u_{i+1}^-)\| \cdot (u_{i+1}^- - u_i^+)\} \tag{52}$$

with the notation

$$u_i^+ \equiv u(x_i + \frac{1}{2}\Delta x_i) \qquad u_{i+1}^- \equiv u(x_{i+1} - \frac{1}{2}\Delta x_i) \qquad a(u_i^+, u_{i+1}^-) = \frac{\partial f(u)}{\partial u} \tag{53}$$

For the case

$$f(u(x,y)) = c_x \cdot u(x,y) \tag{54}$$
$$g(u(x,y)) = c_y \cdot u(x,y) \tag{55}$$

the scheme simplifies to

$$\overline{f}^n(x_{i+\frac{1}{2}}, y_j) = \frac{1}{2}\{c_x u^+(x_i, y_j) + c_x u^-(x_{i+1}, y_j) - \|c_x\|(u^-(x_{i+1}, y_j) - u^+(x_i, y_j))\} \tag{56}$$

The calculation of the numerical fluxes is done in the following steps

1. Reconstruction of the function $u(x, y)$ form its mean-values $\overline{u}_{i,j}$ within the Cell $C_{i,j}$ at the eight Gauß-points

$$P_1 = (x_i - \frac{\Delta x}{2}, y_j - \frac{1}{\sqrt{3}}\frac{\Delta y}{2}) \quad P_2 = (x_i - \frac{\Delta x}{2}, y_j + \frac{1}{\sqrt{3}}\frac{\Delta y}{2})$$
$$P_3 = (x_i + \frac{\Delta x}{2}, y_j - \frac{1}{\sqrt{3}}\frac{\Delta y}{2}) \quad P_4 = (x_i + \frac{\Delta x}{2}, y_j + \frac{1}{\sqrt{3}}\frac{\Delta y}{2})$$
$$P_5 = (x_i - \frac{1}{\sqrt{3}}\frac{\Delta x}{2}, y_j - \frac{\Delta y}{2}) \quad P_6 = (x_i + \frac{1}{\sqrt{3}}\frac{\Delta x}{2}, y_j - \frac{\Delta y}{2})$$
$$P_7 = (x_i - \frac{1}{\sqrt{3}}\frac{\Delta x}{2}, y_j + \frac{\Delta y}{2}) \quad P_8 = (x_i + \frac{1}{\sqrt{3}}\frac{\Delta x}{2}, y_j + \frac{\Delta y}{2})$$

   For this, the reconstruction procedure of section 3.2 is used.

2. Calculation of the numerical fluxes (e. g. in x-direction) at $x = x_i + \frac{1}{2}\Delta x$ with

$$\overline{f}^n(x_{i+\frac{1}{2}}) = [\overline{f}^n(x_{i+\frac{1}{2}}, y_j - \frac{1}{\sqrt{3}}\frac{\Delta y}{2}) + \overline{f}^n(x_{i+\frac{1}{2}}, y_j + \frac{1}{\sqrt{3}}\frac{\Delta y}{2})] \cdot \frac{1}{2}\Delta y \tag{57}$$

The extension of this algorithm to the system of the Euler equations is straightforward. For the Euler equations, a first-order numerical flux-function is defined by:

$$\overline{F}(x_{i+\frac{1}{2},j}) = \frac{1}{2}[\vec{F}(\vec{w^l}) + \vec{F}(\vec{w^r}) - |\underline{A}|(\vec{w^r} - \vec{w^l})] \tag{58}$$

where $\vec{w}_r$ is the vector of the primitive vaiables at the point (x_{i+1}, y_j), $\vec{w}_l$ the corresponding vector at the point (x_i, y_j) and $\underline{A}$ is the Roe-matrice [16]. Evidently, a high-order approximation of the numerical fluxes at the Gauß-point P_3 is given by:

$$\overline{F}(P_3) = \frac{1}{2}[\vec{F}(\vec{w}^r_{i+1,j}(P_3)) + \vec{F}(\vec{w}^l_{i,j}(P_3)) - |\underline{A}|(\vec{w}^r_{i+1,j} - \vec{w}^l_{i,j})] \tag{59}$$

Here $\vec{w}^r_{i+1,j}(P_3)$ denotes the value of the reconstruction polynomial of the cell $C_{i,j}$ (as given in section 3.2) at the Gauß-point P_3. The numerical fluxes are then computed by

$$\overline{F}(x_{i+\frac{1}{2}}) = [\overline{F}(P_3) + \overline{F}(P_4)] \cdot \frac{1}{2}\Delta y \tag{60}$$

with fourth-order accuracy, if the reconstruction is fourth-order accurate.

3.5 Computation of the viscous fluxes

The final goal of the study is to solve numerically the Navier-Stokes equations. In the last sections, the implementation of the convective fluxes and the artificial viscosity was given. Now, a fourth-order accurate finite-volume formulation for the implementation of the viscous fluxes is shown.

The most natural way to approximate the viscous fluxes is to use centred formulae. Doing this properly requires to reconstruct the primitive variables for a second time with a centred stencil. This second reconstruction of the primitive variables doubles the CPU-cost. In order to avoid this, one would like to use the already computed piecewise constant reconstruction polynomials for the computation of the viscous fluxes.

One can not exclude, that the use of the reconstruction-polynomials of the computation of the Euler-fluxes for the computation of the viscous fluxes

causes trouble. The first reason for this is, that if one uses these reconstruction polynomials for the computation of the viscous fluxes, very often non-centred formulae will be used, which is not wanted. Furthermore these reconstruction polynomials are - by construction - discontinuous at the cell-interfaces. For the computation of the viscous fluxes, a discontinuous reconstruction is not reasonable. It is true, that choosing the mean-value of the two approximations at a cell-interface gives a high-order approximation of the value of the function be reconstructed at the cell-interface, but this does not remove the discontinuous character of the reconstruction.

Those are the reasons, why the primitive variables are reconstructed for a second time with a centred stencil. There should be some more efficient possiblities to obtain high-order accurate approximations of the primitive variables at the cell-interfaces with centred formulae, but they are not instantly visible. This point needs in any case further investigation.

For the computation of the shear-stresses, the derivatives of the velocities and the temperature must be known with fourth-order accuracy at the cell-interfaces. They will be obtained with high-order centred differences formulae. The starting-points of these formulae are the high-order approximations of the primitive variables at the Gauß-points. The distribution of the Gausß-points, denoted by $g_{i,1,j}, g_{i,2,j}$, is shown in Fig. 4 For the computation of the first derivative $\frac{\partial u}{\partial x}|_{g_{i,1,j}}$ the following formula is used.

$$\frac{\partial u}{\partial x} = \frac{-u_{g_{i+2,1,j}} + 8u_{gi+1,1,j} - 8u_{g_{i-1,1,j}} + u_{g_{i-2,1,j}}}{12 \cdot \Delta x} + O(\Delta x)^4 \qquad (61)$$

For the computation of $\frac{\partial u}{\partial y}|_{g_{i,1,j}}$ a similar formula is used. But one has to take into account, that the Gauß-points are not equidistantly distributed even if an equidistant grid is used. There are two possibilities to overcome this difficulty: The first is to use fourth-order accurate finite-differences formulae, adapted for variable grids. Those formulae can be obtained with computer-algebra, but they are extremely long and consequently time-consuming. The second possibility is to use only every second Gauß-point for the computation of the derivaties. These points are equidistant if a equidistant grid is used. One finds (for a fourth-order approximation).

$$\frac{\partial u}{\partial y} = \frac{-u_{g_{i,1,j+2}} + 8u_{gi,1,j+1} - 8u_{g_{i,1,j-1}} + u_{g_{i,1,j-2}}}{12 \cdot \Delta y} + O(\Delta y)^4 \qquad (62)$$

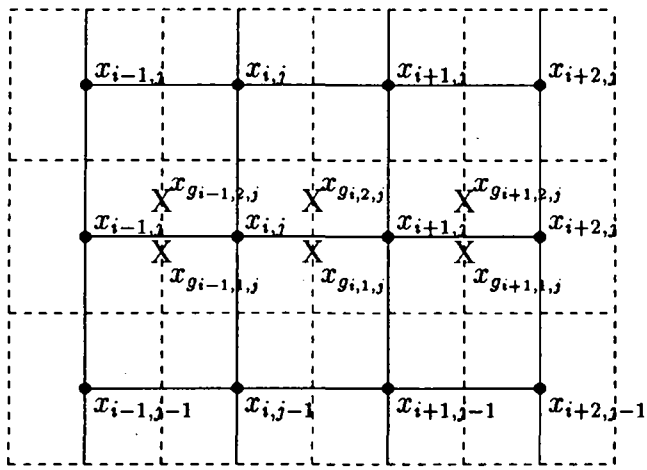


Figure 4: Computational grid and Gauß-points for the computation of the viscous fluxes

Now the integral of the viscous fluxes can be evaluated with fourth-order accuracy as in the previous section.

3.6 Time-integration

The simplest method for time-integration is an explicit Runge-Kutta-Multistep scheme. In general, these schemes provide a possibility to solve numerically equations of the ODE-type

$$\frac{\partial \overline{u}_{i,j}}{\partial t} = \mathcal{L}(\overline{u}_{i,j}) \tag{63}$$

Here $\mathcal{L}$ is a spatial operator. The discretized form of eq. (63) is

$$\overline{u}_{i,j}^{n+1} = \overline{u}_{i,j}^{n} + \Delta t \cdot L(\overline{u}_{i,j}^{n}) \tag{64}$$

where $L(\overline{u}_{i,j}^{n})$ is a numerical approximation of $\mathcal{L}(\overline{u}_{i,j})$. The general explicit Runge-Kutta multistep scheme for eq. (64) is

$$\begin{aligned} \overline{u}_{i,j}^{(l)} &= \overline{u}_{i,j}^{(0)} + \Delta t \sum_{k=0}^{l-1} c_{l,k} L(\overline{u}_{i,j}^{(k)}) \qquad && l = 1 \cdots m \\ \overline{u}_{i,j}^{(0)} &= \overline{u}_{i,j}^{(n)} && \overline{u}^{m} = \overline{u}^{n+1} \end{aligned} \tag{65}$$

The number of intermediate steps is denoted by m. The number of intermediate steps and the coefficients $c_{l,k}$ (to be specified) determine the properties of the scheme. The schemes used in this report were obtained by Shu and Osher [20] under the constraints that the whole scheme (understood as temporal and spatial discretization) is TVD and of the desired order of accuracy in space and time. The restriction on the maximum time-step Δt_0 due to the CFL-condition inherent in all explicit time-stepping schemes was also considered. More precisely, they have shown, that if the scheme (64) is TVD for $\Delta t \leq \alpha \Delta t_0$, where the number α is detemined by the $c_{l,k}$'s. Now, we give some examples that have been used for the computations of this report.

Shu and Osher found the following 2nd order Runge-Kutta 2-step method, denoted by RK2 in the future. It is stable under the condition $\alpha = 1$ (there is no additional restriction of the time step).

$$\overline{u}_{i,j}^{(0)} = \overline{u}_{i,j}^{n} \tag{66}$$

$$\overline{u}_{i,j}^{(1)} = \overline{u}_{i,j}^{(0)} - \Delta t L(\overline{u}_{i,j}^{(0)}) \tag{67}$$

$$\overline{u}_{i,j}^{(2)} = \frac{1}{2}\overline{u}_{i,j}^{(0)} + \frac{1}{2}\overline{u}_{i,j}^{(1)} + \frac{1}{2}\Delta t L(\overline{u}_{i,j}^{(1)}) \tag{68}$$

$$\overline{u}_{i,j}^{n+1} = \overline{u}_{i,j}^{(2)} \tag{69}$$

In [20] a third order Runge-Kutta 3-step scheme in time is presented. It will be denoted by RK3. It is

$$\overline{u}_{i,j}^{(0)} = \overline{u}_{i,j}^{n} \tag{70}$$

$$\overline{u}_{i,j}^{(1)} = \overline{u}_{i,j}^{(0)} - \Delta t L(\overline{u}_{i,j}^{(0)}) \tag{71}$$

$$\overline{u}_{i,j}^{(2)} = \frac{3}{4}\overline{u}_{i,j}^{(0)} + \frac{1}{4}\overline{u}_{i,j}^{(1)} + \frac{1}{4}\Delta t L(\overline{u}_{i,j}^{(1)}) \tag{72}$$

$$\overline{u}_{i,j}^{(3)} = \frac{1}{3}\overline{u}_{i,j}^{(0)} + \frac{2}{3}\overline{u}_{i,j}^{(2)} + \frac{2}{3}\Delta t L(\overline{u}_{i,j}^{(2)}) \tag{73}$$

$$\overline{u}_{i,j}^{n+1} = \overline{u}_{i,j}^{(3)} \tag{74}$$

Stability is obtained without any additional condition (i. e. $\alpha = 1$)

For practical calculations, we have assumed that a linear analysis of stability was valid. This means that the linear Courant-Friedrichs-Levy criterion was used. For the simple advection equation it is given by $\Delta t \leq |c| \Delta x$.

3.7 Stability properties of ENO-schemes

As ENO schemes use an adaptive stencil, a rigorous analysis of stability is complicated. A rigorous analysis of stability of third-order accurate ENO-scheme was done in [14], using the linear one-dimensional advection equation

$$\frac{\partial u}{\partial t} + c\frac{\partial u}{\partial x} = 0 \tag{75}$$

It was shown that for $c > 0$ the scheme is always stable if the CFL-number fullfills the condition $CFL < 0.6$.

In [13] a different approach to this issue is shown. If one uses as initial condition the function

$$u(x) = u^0(x) = \exp(-x) \tag{76}$$

the ENO-procedure is going to use at the beginning of the computation a stencil that is oriented to the right. So a linear analysis of stability can be done at least for the first time-steps of the computation with a fixed stencil. For details see [13]. The results of the stability analysis reported there for 2nd order ENO-schemes can be resumed as:

- for $c > 0$, fixed stencil schemes are always instable, but the amplification factors do not exceed much the critical value
- for $c < 0$, stability is obtained for $CFL < 0.5$

Computations with fixed stencils show an obvious tendency to instability, while adaptive stencil computations deliver stable results [13]. This indicates that the adaptation of the stencil ensures the stability of ENO-schemes.

3.8 On the precision of ENO-schemes

Formally, ENO-schemes can be extended to any desired order of accuracy. But there are some well-known cases, where even for the linear advection equation (75) severe problems come up and ENO-schemes do not have the desired order of accuracy. The loss of precision is can only be seen if relatively

fine grids are used in grid-refinement- studies. There are two well-known test-problems for this subject:

$$u(x,0) = \sin^4(x) \qquad \text{or} \qquad u(x,0) = \exp(-x) \tag{77}$$

One instructive explanation for this behaviour was given by Shu [21]. He observed for cases like $u(x,0) = \exp(-x)$, that the ENO-adaption procedure uses for a certain time an unstable stencil. So oscillations occur during computation. Only when the oscillations become too severe, the ENO-scheme is going to stabilize the scheme automatically by changeing the stencil. The price that one has to pay for this stabilisation of the scheme is a loss of precision.

Several remedies are proposed to overcome this difficulty. It seems, that until now, no standard-remedy was found. There are several concurrent ideas which all have in common, that the choice of the stencil must be changed in a way, that the stencil is biased towards a stencil that is stable in the sense of linear analysis of stability. For details see [17], [21] and [3], where the authors report more or less encouraging results.

The extension of ENO-schemes to the Euler- or Navier-Stokes equations and its application to fluid-mechanics seems sometimes to make problems. Erlebacher et al. [6] report, that they cannot use the Navier-Stokes equations in conservative form to get reasonable results in shear-flow problems. Atkins [3] shows good results on shear-flow problems with 3rd- and 5th order ENO, but does not report 4th order results. He uses a modified ENO scheme. Casper and Atkins [5] show good results for flow over a ramp with 3rd order ENO.

4 Results

4.1 Physical problem

The basic flow is defined by a hyperbolic tangent velocity profile and is given by:

$$u_b = \frac{1}{2}\tanh(2y) \tag{78}$$

$$T = 1 + \frac{\gamma - 1}{2} \cdot \left(\frac{Ma}{2}\right)^2 \cdot (1 - (2u_b)^2) \tag{79}$$

$$\rho = \frac{1}{T} \tag{80}$$

$$p = \frac{1}{\gamma Ma^2} \tag{81}$$

A small deterministic perturbation is added to this basic flow:

$$u = \frac{\epsilon y \lambda}{20\pi} \cdot \sin(\frac{2\pi x}{\lambda}) \cdot \exp(-\frac{1}{10}y^2) \tag{82}$$

$$v = \frac{\epsilon}{2} \cdot \cos(\frac{2\pi x}{\lambda}) \cdot \exp(-\frac{1}{10}y^2) \tag{83}$$

It is easily verified that $\vec{\nabla} \cdot \vec{u} = 0$. λ is the dimensionless wavelength of the perturbation. $\epsilon = 0.1$ is the amplitude of the deterministic perturbation.

The boundary conditions are the following:

- periodic in x:

$$\vec{q}|_{x=0} = \vec{q}|_{x=L_x} \qquad \left.\frac{\partial^n \vec{q}}{\partial x^n}\right|_{x=0} = \left.\frac{\partial^n \vec{q}}{\partial x^n}\right|_{x=L_x} \tag{84}$$

- slip conditions on the upper and lower boundary

$$\left.\frac{\partial \rho}{\partial y}\right|_{y=\pm L_y} = 0 \qquad \left.\frac{\partial p}{\partial y}\right|_{y=\pm L_y} = 0 \qquad \left.\frac{\partial u}{\partial y}\right|_{y=\pm L_y} = 0 \qquad v|_{y=\pm L_y} = 0 \tag{85}$$

Treatment of the cells close to the boundaries for the third-order ENO-scheme:

In x-direction, no special treatment of the cells near the boundaries is necessary, as periodicity of the n-th derivative is supposed. On the contrary, in y-direction the order of reconstruction must be reduced to second order for for the cells $j = 1$ and $j = jmax - 1$. For the cell $j = 0$ and $j = jmax$, the solution of $j = 1$ and $j = jmax - 1$ is linaerly extrapolated with first order accuracy.

The reason for this reduction is the following: As shown in section 3.7 a reconstruction with a fixed stencil can produce instabilities. For the cell $j = 1$ the stencil cannot be shifted two times downwards, as the cell $j = -1$ does not exist. But a correct treatment of the ENO-procedure requires the possibility of shifting two-times downwards. On the other side, a second-order reconstruction is possible as for the cell $j = 1$ as the ENO-reconstruction only requires one shift. A similar treatment is applied to the cell $j = jmax - 1$

In all computations a cartesian mesh was used. The grid is uniform in the x-direction and either uniform or stretched in the y-direction. So one gets for the mesh-sizes:

$$\Delta x = \frac{L_x}{N_x} = const. \tag{86}$$

while Δy is either

$$\Delta y = \frac{2 \cdot L_y}{N_y} = const. \tag{87}$$

or defined by a stretching parameter (see section 4.4) and N_x and N_y are the number of points in horizontal and vertical direction. The number of points varied from 101 to 251 points in x- and from 101 to 201 points in y-direction.

4.2 Tools for analysing the flow-field

The flow will be analysed with energy-spectra. They are obtained by:

$$e(k) = \frac{1}{2L_y} \int_{-L_y}^{L_y} |\hat{u}(k,y)|^2 + |\hat{v}(k,y)|^2 dy \tag{88}$$

where $\hat{u}(k,y)$ and $\hat{v}(k,y)$ are the Fourier-transforms of the horizontal and vertical components of the velocity-vector:

$$\hat{u}(k,y) = \frac{1}{L_x} \int_0^{L_x} u(x,y) \cdot exp(ikx) dx \tag{89}$$

$$\hat{v}(k,y) = \frac{1}{L_x} \int_0^{L_x} v(x,y) \cdot exp(ikx) dx \tag{90}$$

The coefficients $\hat{u}(k,y)$ and $\hat{v}(k,y)$ are approximated numerically with a fast-Fourier-routine (FFT). The integral $e(k)$ is approached by a simple quadrature formula. The numerical approximation of $e(k)$ is E_l, where the index l is a normalised wave-number. The relation between l and k is $l = \frac{L_x}{2\pi} \cdot k$. In the future especially the time-evolution of the mode $l = 1$ $(E_1(t))$ will be investigated.

4.3 Simulations at transonic Mach numbers with one vortex

The parameters for those simulations are

$$Ma = 1.6 \ (i.e. Ma_c = 0.8), \qquad Re = 400, \qquad Pr = 1.0, \qquad (91)$$
$$L_x = 20, \qquad L_y = 10, \qquad \lambda = 20.$$

An often-used measure for the shear-layer thickness is the vorticity thickness, defined as

$$\delta_\omega = \frac{u_\infty - u_{-\infty}}{|\frac{\partial}{\partial y}\frac{\overline{\rho u}}{\overline{\rho}}|_{max}} \qquad (92)$$

The grid is cartesian, equidistant in x- and y-direction. Fig. 5 shows the time-evolution of the vorticity thickness of a 3rd order ENO-scheme, a 2nd order MUSCL-scheme and a spectral method (before shocks appear). Until $T \simeq 40$ (the time when shocks comes up and spectral methods fail), the three schemes show the same results. When shocks appear, a small difference between ENO- and MUSCL-schemes is observed. ENO detects the maximum vorticity-thickness at $T \simeq 72$ while MUSCL detects it at $T \simeq 78$. In the same figure, several runs with ENO-schemes and refined grids are shown. It seems that computations with $151 * 151$ grid-points are grid-independent.

The Fig. 6 shows the contour-lines of density, temperature, Mach number and entropy at the time $T = 80$ obtained with a MUSCL-scheme, Fig. 7 shows the corresponding contour-lines for a 3rd order ENO computation. The shocks are well resolved with both schemes, the oscillations are small. But obviously, the 3rd order ENO-scheme is less oscillatory than the MUSCL-scheme. It seems also that the contact-discontinuities are better resolved with ENO-schemes.

Figure 5: Evolution of vorticity thickness for MUSCL, ENO and spectral, $Ma_c = 0.8$, $Re = 400$, $Pr = 1.0$, $L_x = 20 \cdot \delta_i$

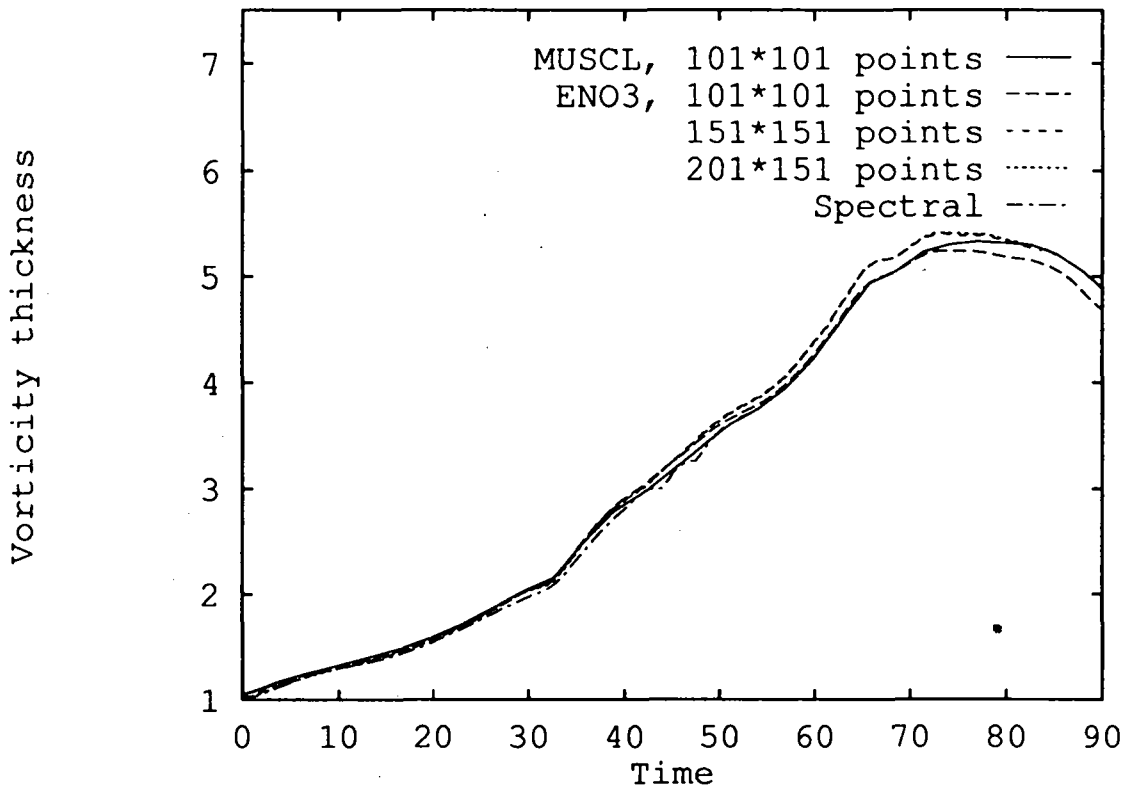


Figure 6: Contour-lines of MUSCL-scheme, 101*101 points, $Ma_c = 0.8$, $Re = 400$, $Pr = 1.0$, $L_x = 20 \cdot \delta_i$, $t = 80$

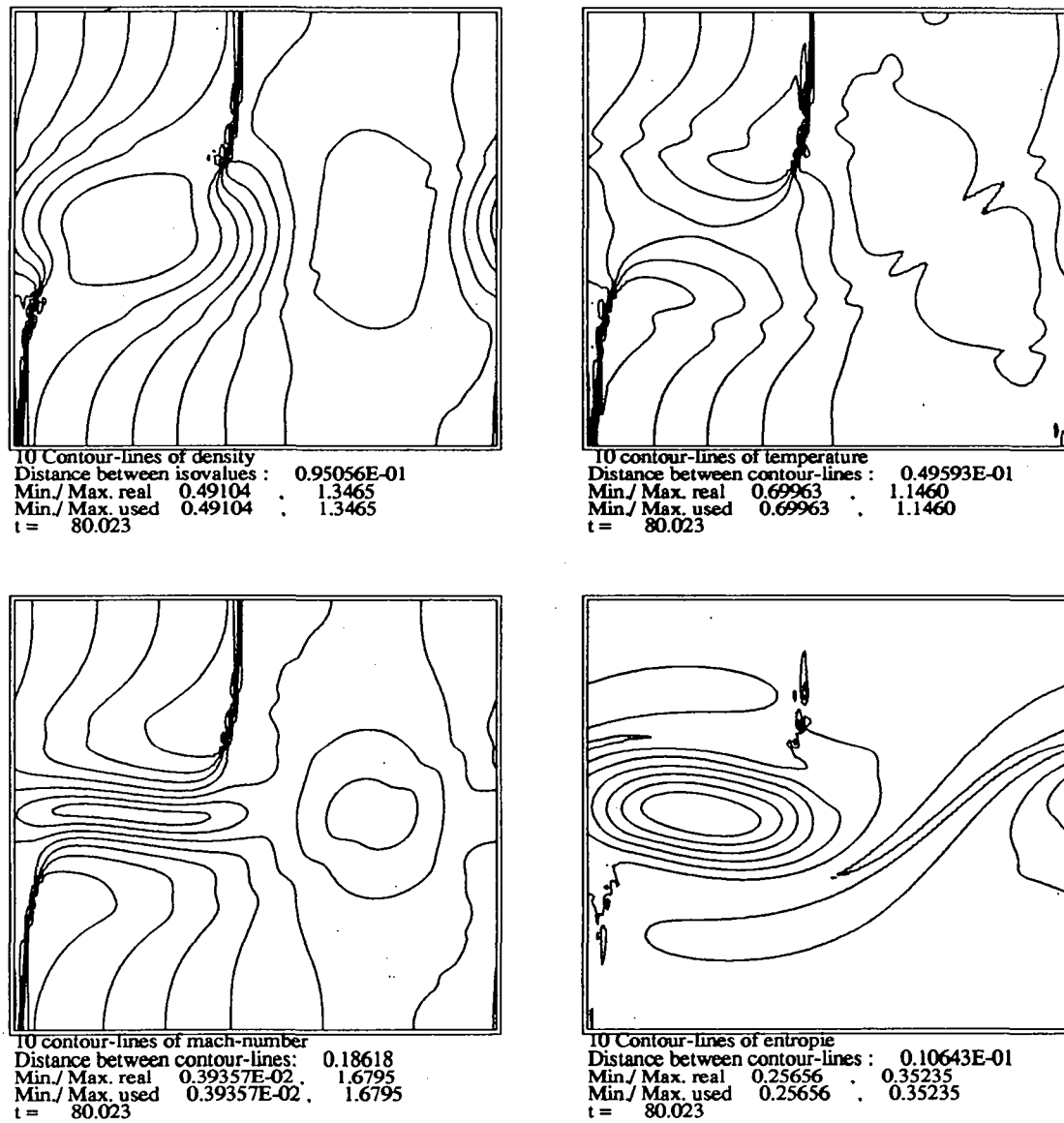
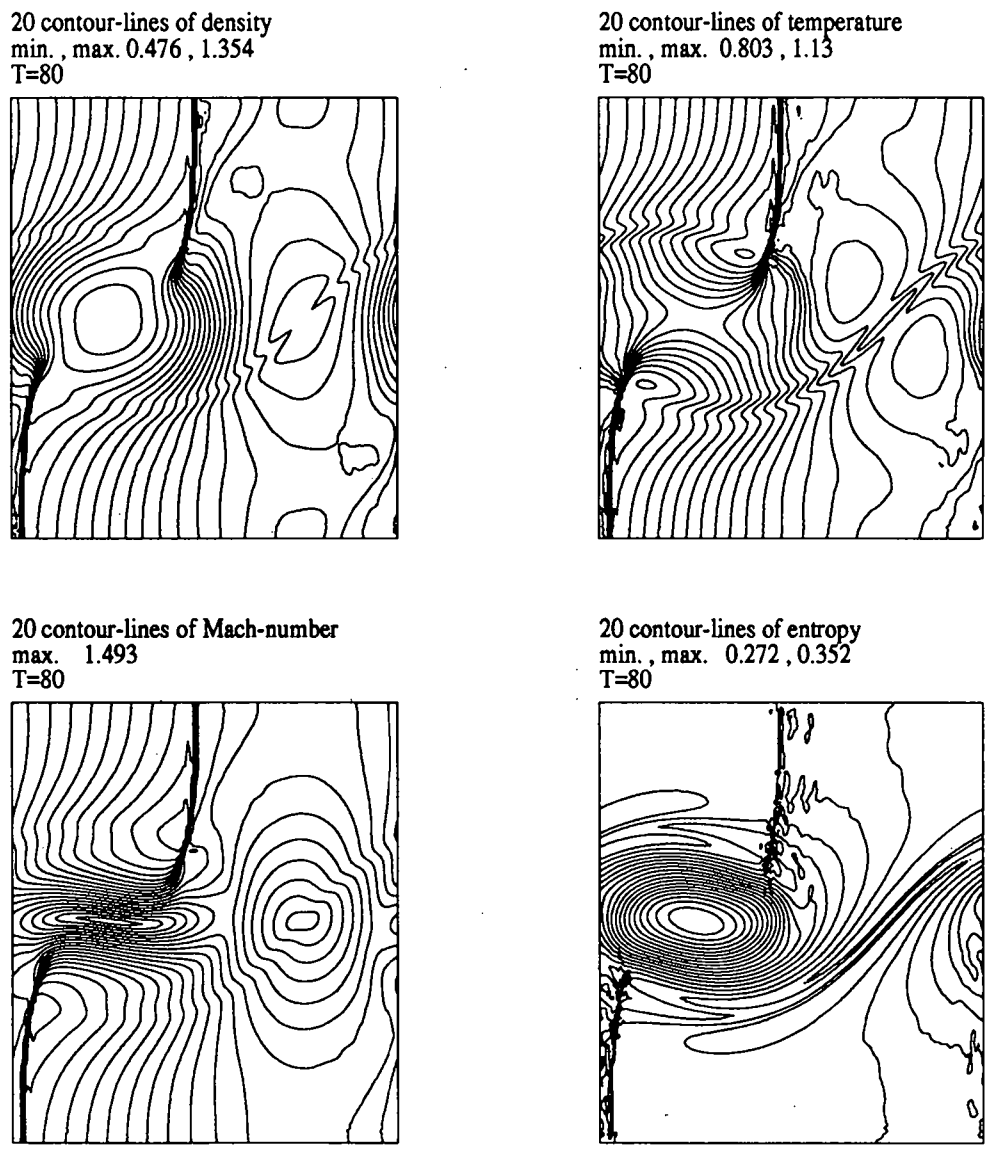


Figure 7: Contour-lines of 3rd order ENO, 101*101 points, $Ma_c = 0.8$, $Re = 400$, $Pr = 1.0$, $L_x = 20 \cdot \delta_i$, $t = 80$



4.4 Simulations at transonic Mach numbers with two vortices

The parameters of the simulations are

$$\begin{aligned} Ma = 1.6 \ (i.e. Ma_c = 0.8), \qquad & Re = 1000, \qquad Pr = 0.7, \\ L_x = 22.52, \qquad & L_y = 22.52 \qquad \lambda = 11.26 \end{aligned} \tag{93}$$

The grid is a cartesian grid, equidistant in x-direction, and stretched in y-direction. The stretching in y-direction is obtained by a transformation of co-ordinates:

$$y_1 = -1 + \frac{2}{N_y} \tag{94}$$

$$y = L_y[(1-\alpha) \cdot y_1^3 + \alpha \cdot y_1] \tag{95}$$

The parameter α determines the stretching of the grid. In this simulation, $\alpha = 0.5$ was used. The number of grid-points is $N_x = 101$ and $N_y = 101$ points. This grid was used in the spectral-computations of [7], where the parameter α was adjusted by the auto-adaptive spectral method presented in this work.

In this computation, only the mode $\lambda = 11.26$ is exited. Especially the mode $\lambda = L_x = 22.52$, the mode which forces the pairing, is not exited. One is interested, whether the pairing-forcing mode is amplified in an unphysical way due to numerical dissipation, as it was already observed in [2] and [12]. If so, one wants to know, how behaves the ENO-scheme.

Fig. 8 shows the time-history of the vorticity-thickness for a 2nd order MUSCL- and a 3rd order ENO-scheme. There is a clear separation of the curves. Until $T \simeq 80$ the two graphs give nearly the same results: a small peak appears at $T \simeq 60$ indicating the creation of two distinct vortices, what is expected from linear analysis of stability. Afterwards the graphs differ enormously. But the two curves exhibit a big maximum at a later time, indicating the vortex-pairing. This is shown in Fig. 9 and 10 where the contour-lines of density and vorticity for MUSCL- and ENO-schems at the times $T = 180$ (for MUSCL-schemes) and $T = 300$ (3rd order ENO) are shown. It seems that the time when the vortex-pairing occurs depends essentially on the precision of the numerical method.

Figure 8: Evolution of vorticity thickness for MUSCL, ENO, $Ma_c = 0.8$, $Re = 1000$, $Pr = 0.7$, $L_x = 15.06 \cdot \delta_i$

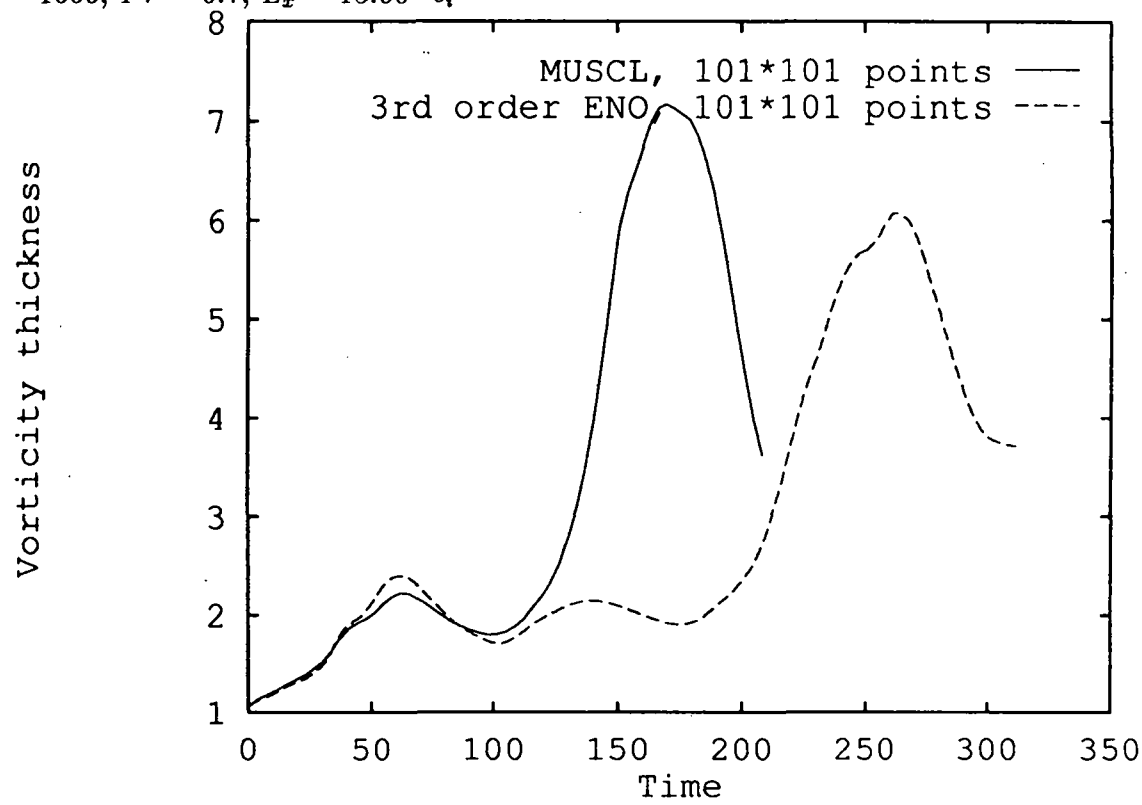
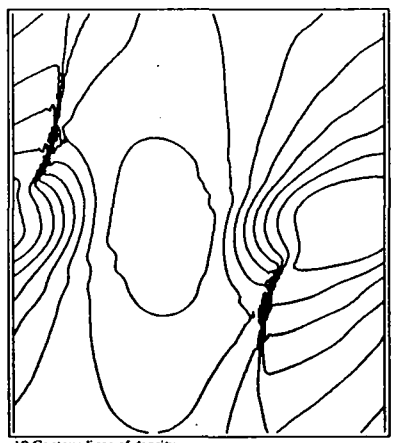
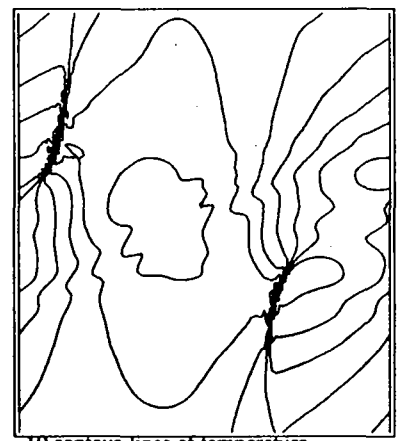
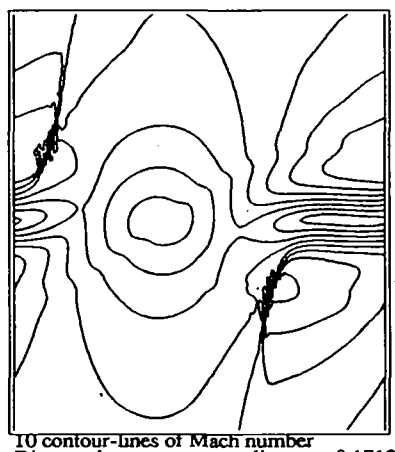


Figure 9: Contour-lines of the MUSCL-scheme, 101× 101 points, $Ma_c = 0.8$, $Re = 1000$, $Pr = 0.7$ $L_x = 22.52 \cdot \delta_i$, $T = 180$







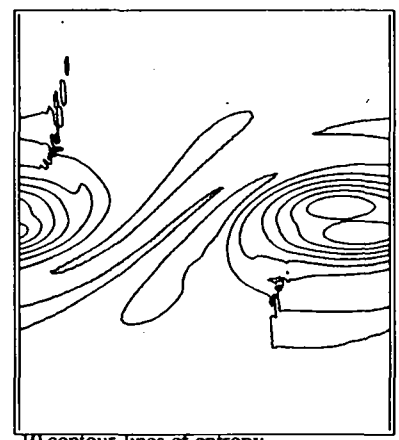
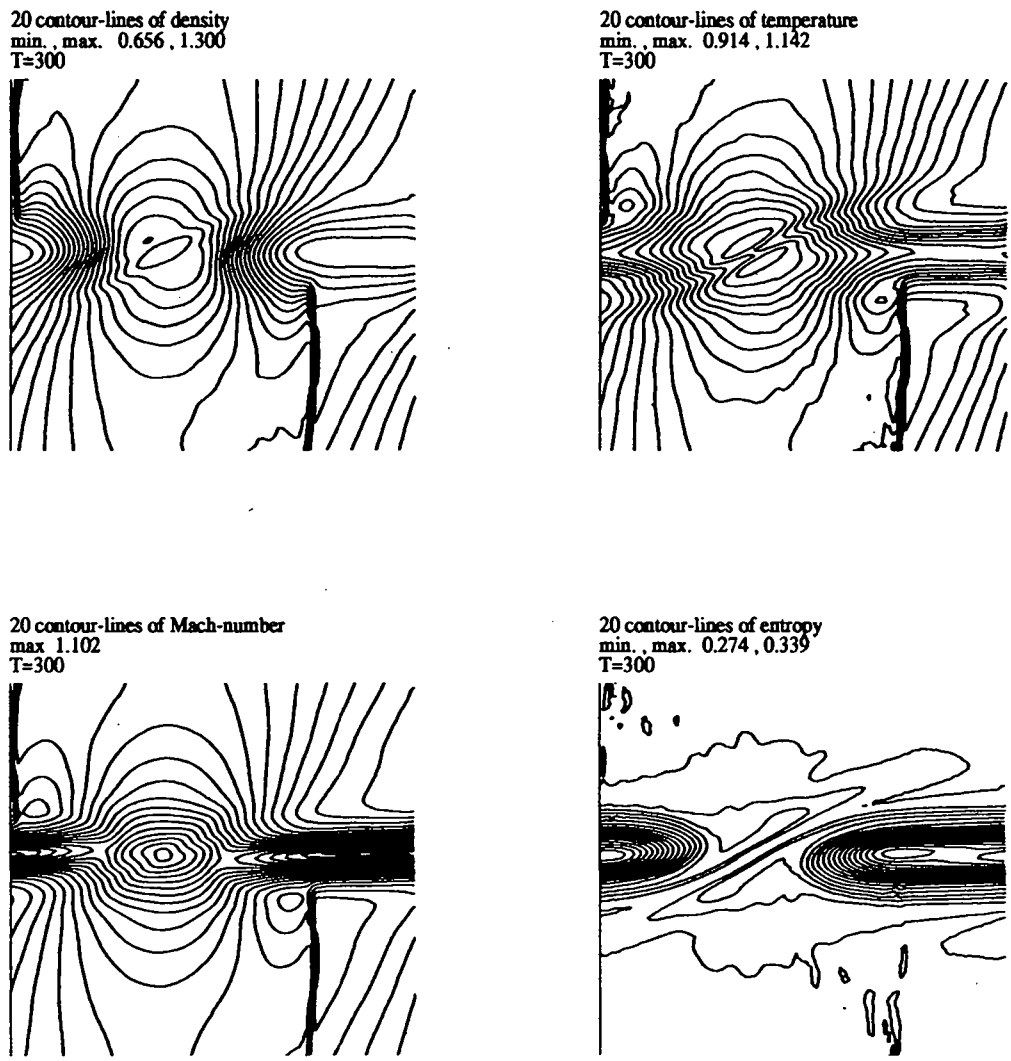


Figure 10: Contour-lines of 3rd order ENO, 101 points in x-direction, $Ma_c = 0.8$, $Re = 1000$, $Pr = 0.7$, $L_x = 22.52 \cdot \delta_i$, $t = 300$



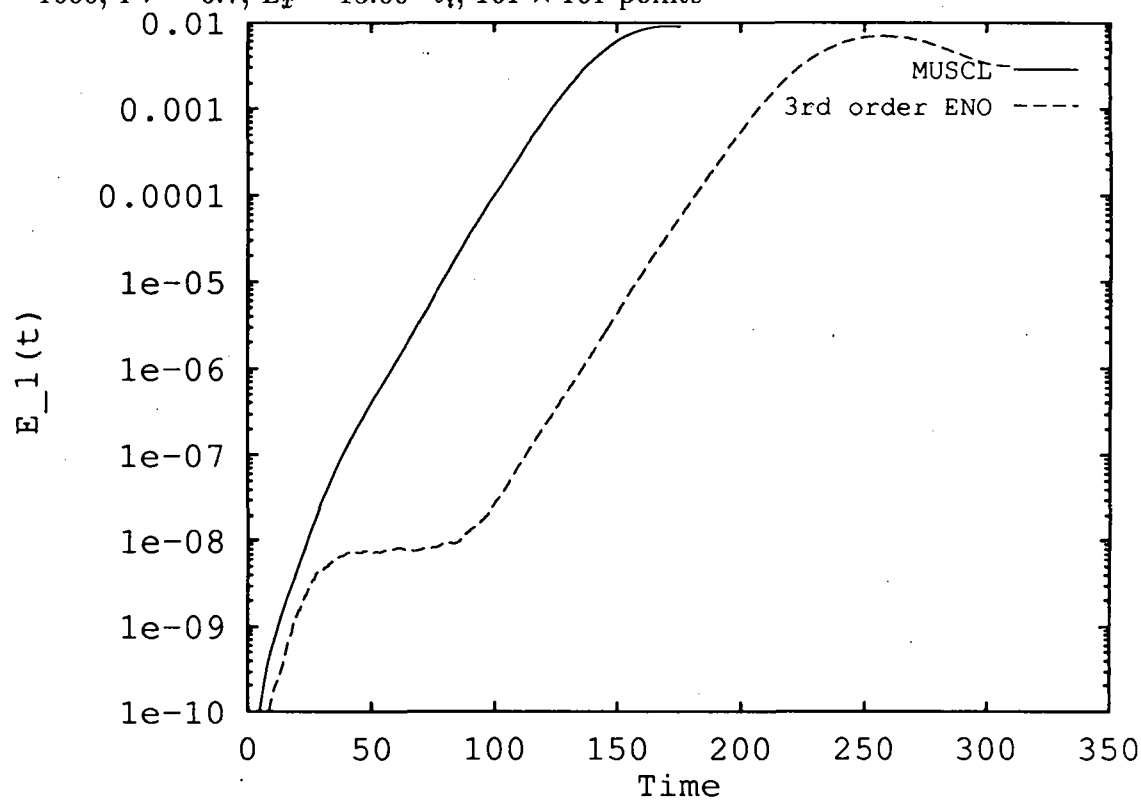
These results compare well with those of [2] and [12]. Now, have a look at the energy-spectra for a more detailed investigation of this issue.

Fig. 11 shows the time-evolution of the mode E_1, which is the interaction-forcing mode, for MUSCL- and ENO-schemes for a $101 * 101$ points computation on a semi-logarithmic scale. The difference between MUSCL- and ENO-schemes is obvious. The MUSCL-scheme exhibits an unphysical amplification-rate at the beginning of the computation. After a certain threshold, linear growth starts. ENO also shows a nonphysical amplification-rate at the beginning of the computation, but develops a plateau at a very low level (much less than the truncation error) and then linear growth starts. These observations suggest that

- the more precise the solution is, the later the vortex-pairing starts
- MUSCL- and ENO-schemes behave differentely

This will be investigated in the next section at subsonic Mach numbers with grid-refinement studies.

Figure 11: Time-evolution of the mode E_1 for MUSCL and ENO, $Ma_c = 0.8$, $Re = 1000$, $Pr = 0.7$, $L_x = 15.06 \cdot \delta_i$, 101×101 points



4.5 Simulations at subsonic Mach numbers with two vortices

There are two reasons why these simulations are carried out. The first is that one wants to verify whether the experiences made at $Ma = 1.6$ will also be made qualitatively at $Ma = 0.6$. This should be the case if the governing effect is the artificial viscosity. The second reason is that reference computations with high-resolving spectral-methods, where no explicit numerical dissipation terms are present, can be done.

The dimensionless parameters of the simulations are

$$\begin{aligned} Ma = 0.6 \ (i.e.\ Ma_c = 0.3), \qquad & Re = 1000, \qquad Pr = 0.7, \\ L_x = 15.06, \qquad & L_y = 7. \qquad \lambda = 7.53 \end{aligned} \tag{96}$$

The grids are equidistant in x- and y-direction. The number of points varied from $N_x = 101$ to $N_x = 251$ in x- and in y-direction for the MUSCL-scheme. For ENO, in x-direction the number of points varied from $N_x = 101$ to $N_x = 201$ and in y-direction from $N_y = 101$ to $N_y = 121$. Fig. 12 shows the time-evolution of the vorticity thickness for MUSCL- and ENO-schemes for refined grids. Again a clear separation of the curves can be observed. Until $T \simeq 35$ all curves do not differ, especially the small peak at $T \simeq 20$, indicating the creation of two distinct vortices is represented in the same way by all curves. Afterwards, separation is observed. The position of the second, big peak indicating the vortex-pairing depends essentially on the precision of the solution. Again it seems that the more precise the solution is, the later the vortex-pairing occurs. It seems also, that MUSCL- and ENO-schemes behave in a different way, what was already suspected.

This is confirmed, if one looks at the time-evolution of the pairing-forcing mode E_1 (Fig. 13). For the MUSCL-scheme, the unphysical behaviour of E_1 at the beginning of the computation is obvious. When the amplitude exceeds a certain threshold a linear growth, that is in reasonable agreement with linear theory of stability, starts. It can also be seen from the Figure 13 that the threshold, that has to be trespassed for the start of linear growth becomes lower.

ENO-schemes also show an unphysical behaviour at the beginning of the computation that stops at a relatively low level and is followed by a plateau. Later linear growth, in good agreement with linear theory of stabiliy starts. Grid refinement in Figure 13 shows that the plateau before linear growth starts is lower for finer grids. So indeed, ENO-schemes and MUSCL-schemes behave differentely.

Fig. 14 shows the contour-lines of density, temperature, Mach number and entropy at the time $T = 140$, i. e. when the vortex-pairing was accomplished. The solutions are smooth, without oscillations, all structures are well-resolved.

Note, that the origin of the vortex-pairing, accomplished at $T = 140$ is completely unphysical (numerical dissipation). Fig. 13 and 14 suggest that any kind of perturbation, regardless how was generated, behaves like a physical structure if it is only sufficiently amplified.

Figure 12: Vorticity-thickness for MUSCL and ENO, $Ma_c = 0.3$, $Re = 1000$, $Pr = 0.7$, $L_x = 15.06 \cdot \delta_i$

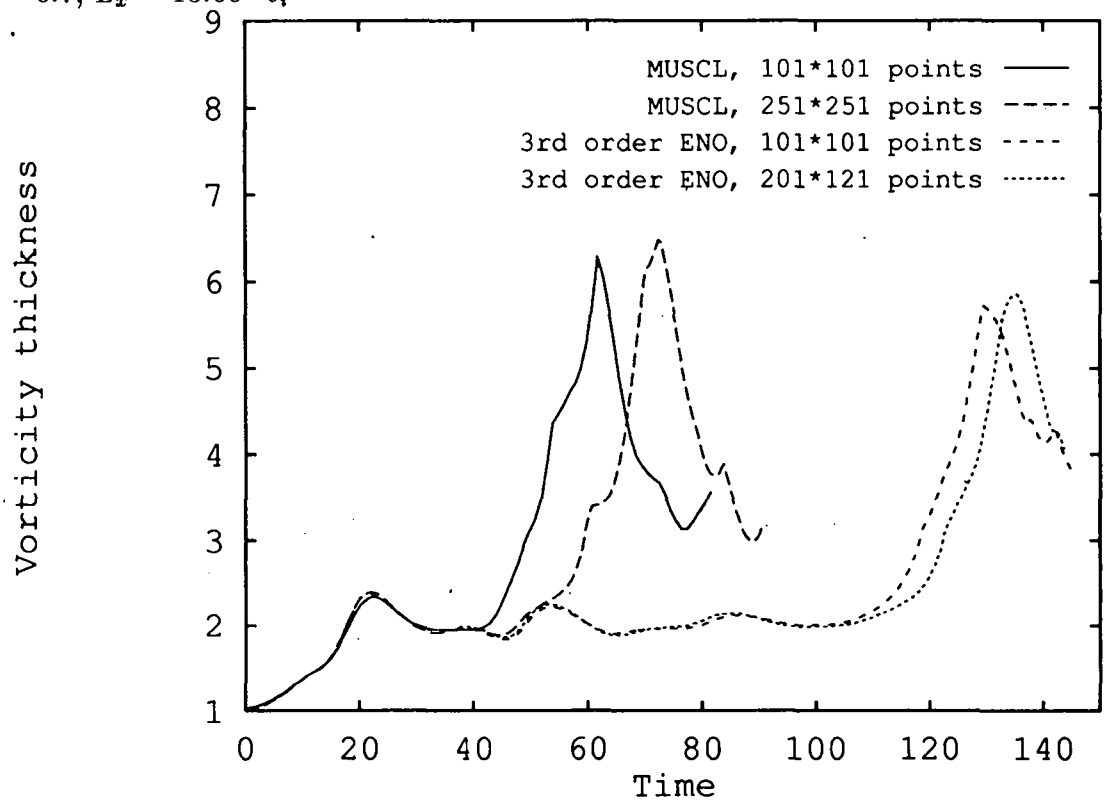


Figure 13: Time history of the mode E_1 for MUSCL, ENO, $Ma_c = 0.3$, $Re = 1000$, $Pr = 0.7$, $L_x = 15.06 \cdot \delta_i$

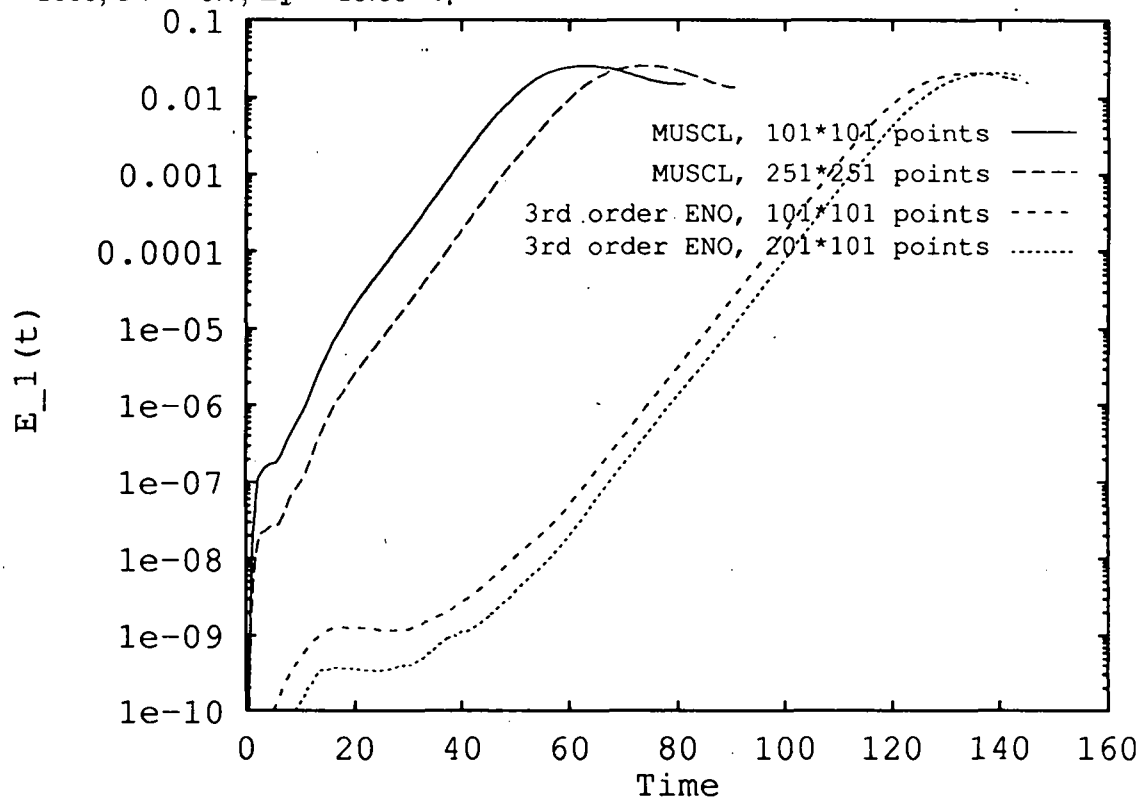
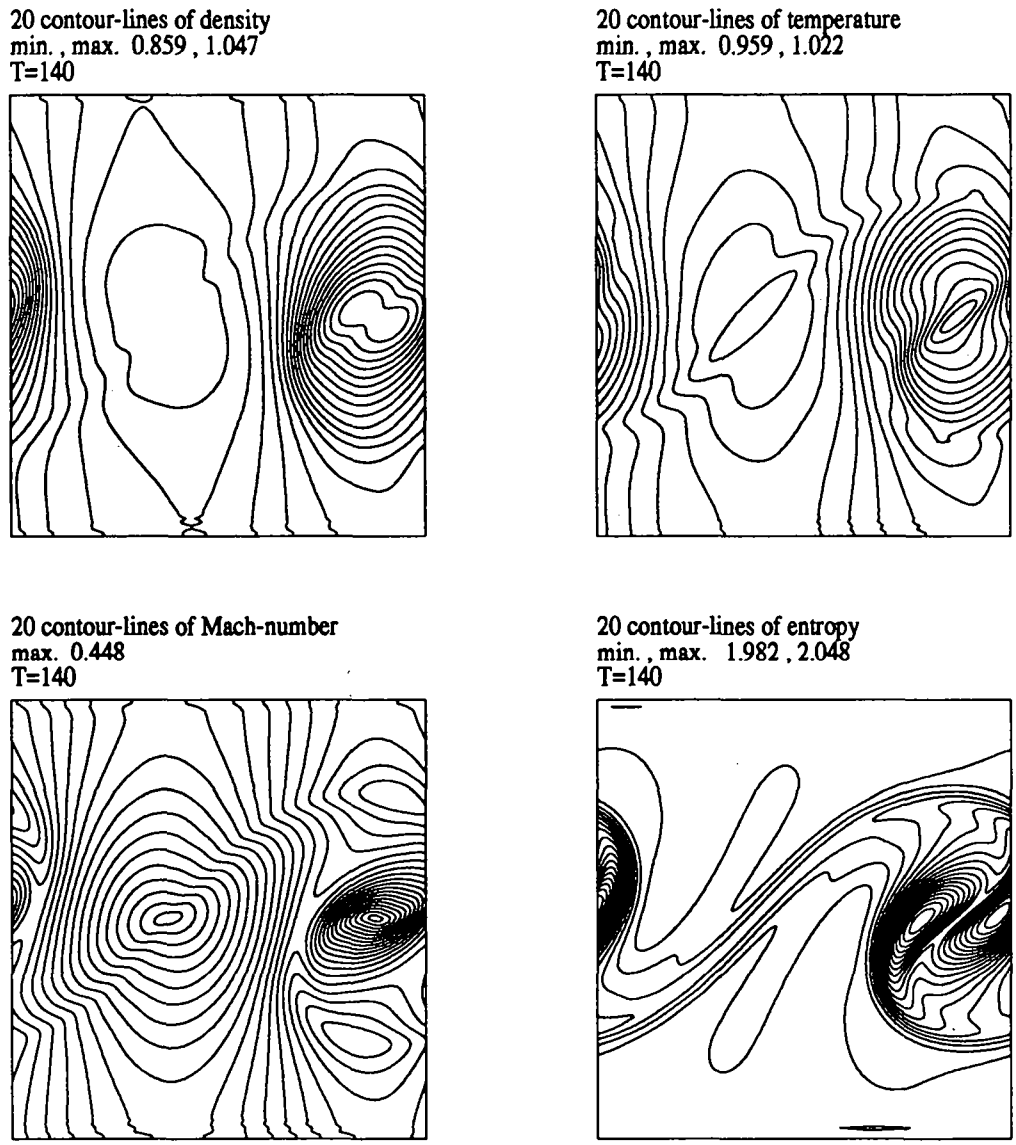


Figure 14: Contour-lines of 3rd order ENO, 101 × 101 points, $Ma_c = 0.3$, $Re = 1000$, $Pr = 0.7$, $L_x = 15.06 \cdot \delta_i$, $t = 140$



4.6 Simulations with 4th-order ENO-schemes

Here some results obtained with a 4th-order ENO-scheme are shown. The simulation is the same as in section 4.3, so the parameters of the simulation are:

$$\begin{aligned} Ma = 1.6 \ (i.e.\ Ma_c = 0.8), \qquad & Re = 400, \qquad Pr = 1.0, \\ L_x = 20, \qquad & L_y = 10, \qquad \lambda = 20. \end{aligned} \tag{97}$$

Fig. 16 shows the contour lines of density, temperature, Mach number and entropy on a 151×151 points grid at the time $T = 40$. In all plots, the oscillations are obvious. No biasing of the stencil was used. This coincides with the experiences of several authors who already have reported difficulties with 4^{th} order accurate ENO-schemes and therefore introduced stencil-biasing [3], [21]. For a 101×101-points grid, reasonable results were obtained. Fig. 15 shows the evolution of the vorticity thickness of 3rd- and 4th-order ENO-schemes with refined grids. The 4th-order ENO computation on a 101×101 points grid coincides well with the 3rd-order computations, while the 4th-order computation on a 151×151 points is not stable for times $T > 70$.

Figure 15: Vorticity-thickness for 3rd- and 4th-order ENO, $Ma_c = 0.8$, $Re = 400$, $Pr = 1.0$, $L_x = 20 \cdot \delta_i$

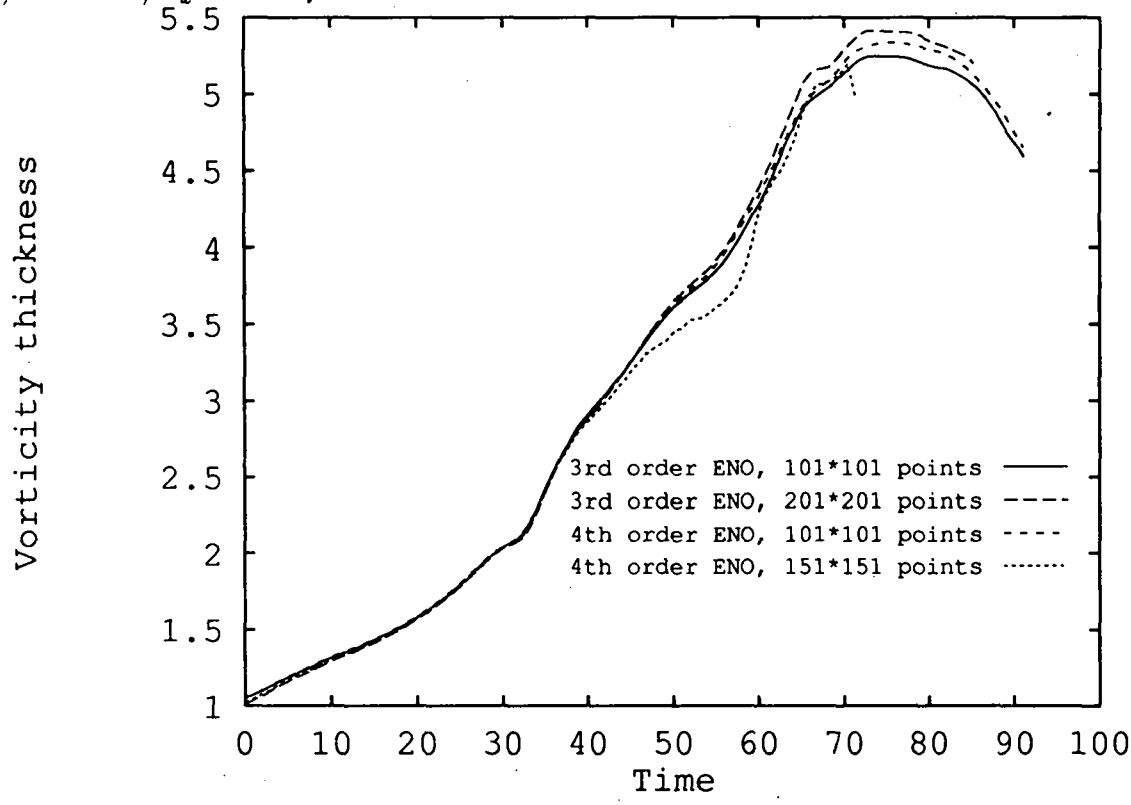
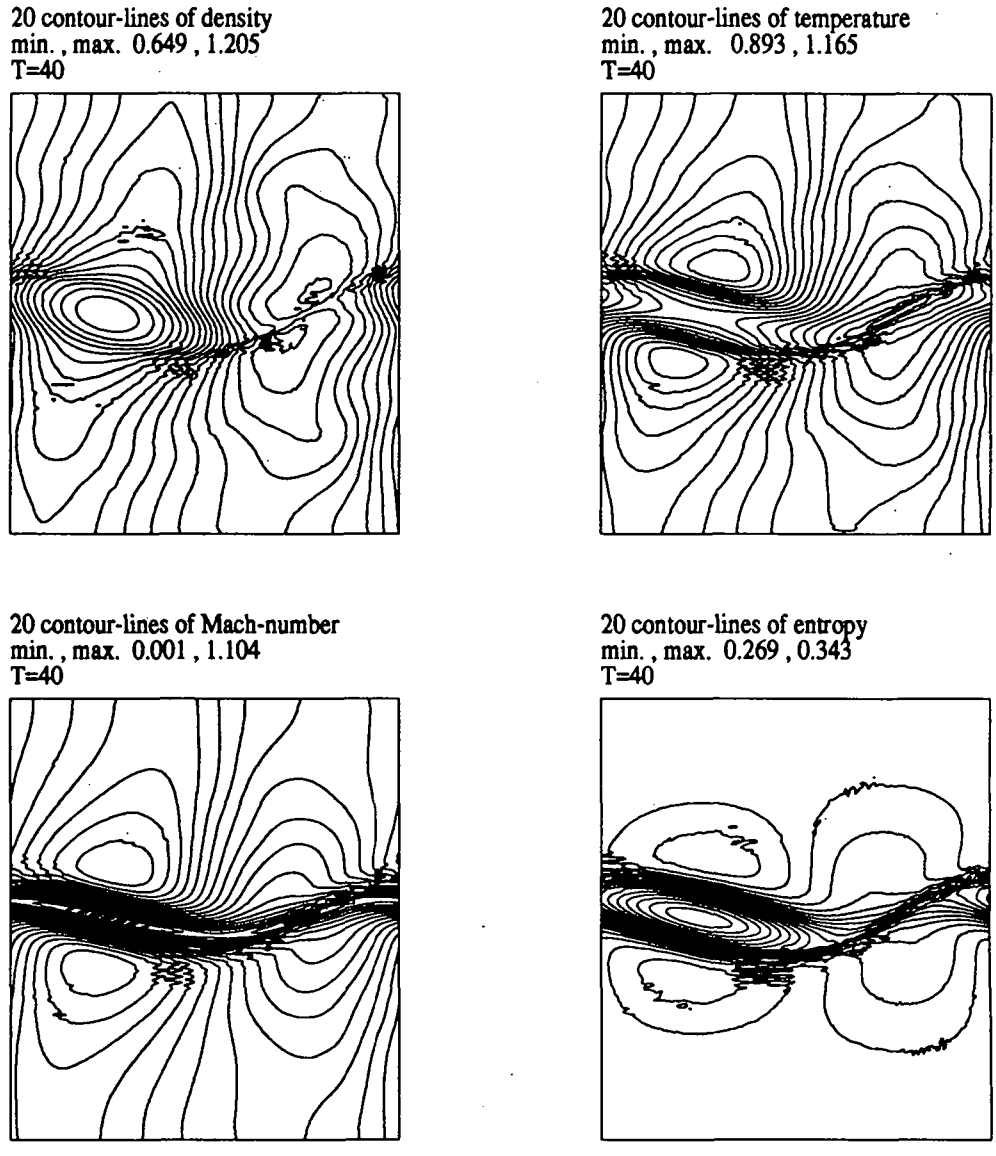


Figure 16: Contour-lines of 4th-order ENO, 151 × 151 points, $Ma_c = 0.8$, $Re = 400$, $Pr = 1.0$, $L_x = 20. \cdot \delta_i$, $t = 40$



5 Conclusion

In this report the influence of different numerical schemes on the results of direct numerical simulation of shear-flow was investigated. In a first part, some results from linear analysis of stability were reported. These results were exploited by several authors for direct numerical simulations. They observed an enormous influence of the numerical viscosity and the precision of the numerical method on the results, if usual 2nd-order accurate MUSCL- or TVD-schemes are used. As high-order schemes should be less dissipative than the usual 2nd order schemes it is natural to apply higher-order schemes to this kind of flow.

In a second section, high-order ENO-schemes and some of their most important properties were given. The most important steps, the reconstruction procedure and the choice of the stencil were discussed. An attempt to understand the stability properties of this new kind of scheme was done. Also, it was reported, that ENO-schemes with higher orders (e. g. 4, 5,..) can not have the desired accuracy.

The algorithm was applied to the full, compressible Navier-Stokes equations in two dimensions. The results of 3rd-order accurate ENO-computations with one structure compare well with those of MUSCL- and spectral-methods.

As for computations with two structures, where only the most amplified mode is exited and the amplitudes of all other modes vanish, it seems that ENO-schemes do not behave in the same manner as MUSCL-schemes. There is a certain tendency indicating, that the more precise the solution is, more trustfull results are obtained. But unfortunately, no grid-independent results can be obtained with ENO-schemes. Computations with spectral-methods on this subject are foreseen.

The computations with 4th-order ENO-schemes make problemes. At the moment computations on fine grids can not be done. It might be that the procedure of adapting the stencil must be changed as it was suggested by several authors. Also the implementation of the computation of the viscous fluxes must be investigated, as the actual procedure doubles the CPU-cost.

Acknowledgments

I am indebted to R. Peyret, H. Guillard and R. Abgrall for a lot of fruitfull discussions, suggestions and continuous encouragement.

References

[1] R. Abgrall, On Essetially Non-oscillatory Schemes on Unstructured Meshes: Analysis and Implementation, accepted for J. Comp. Phys..

[2] H. L. Atkins, Analysis of a second order-accurate finite-volume method for temporally growing compressible shear layers, AIAA Paper No. 89-1809.

[3] H. L. Atkins, High-Order ENO Methods for the Unsteady Compressible Navier-Stokes Equations, AIAA Paper No. 91-1557

[4] W. Blumen, Shear layer instability of an inviscid compressible fluid, J. Fluid Mech., vol 40, part 4, (1970), pp. 769 - 781.

[5] J. Casper and H. L. Atkins, A Finite-Volume High-Order ENO-Scheme for Two-Dimensional Hyperbolic Systems, J. Comp. Phys. 106, (1993) pp. 62 - 76.

[6] C.-W. Shu, G. Erlebacher, T. A. Zang, D. Whitaker and S. Osher, High-Order ENO Schemes Applied to Two- and Three-Dimensional Compressible Flow, ICASE-report 91-38, (1991).

[7] H. Guillard, J. M. Malé and R. Peyret, Adaptive spectral methods with application to mixing layer computations, J. Comp. Phys., vol 102, (1993), pp. 114 - 127.

[8] A. Harten, B. Engquist, S. Osher and S. Chakravarthy, Uniformly High Order Accurate Essentially Non-oscillatory Schemes III, J. Comp. Phys. 71 (1987), pp. 231 - 303.

[9] A. Harten, On high-order accurate interpolation for non-oscillating shock capturing schemes, MRC Technical Summary Report No. 2829, University of Wisconsin, 1985, (unpublished).

[10] H. Helmholtz, Über discontinuierliche Flüssigkeits-Bewegungen, Monatsberichte der kön. preuß. Akad. der Wissenschaften, April 1868, S. 215 - 228.

[11] E. Isaacson, H. B. Keller, Analysis of numerical methods, Wiley & Sons, 1966.

[12] T. Lumpp and H. Guillard, Numerical Simulations of Compressible Mixing Layers, Rapports INRIA Nr. 2217, (1994).

[13] T. Lumpp, A Note on High-order ENO-schemes Applied to the Advection Equation, INRIA, internal report.

[14] A. Merlo, Méthodes numériques pour le calcul d'écoulements hypersoniques stationnaires en deséquilibre thermique ou instationnaire à l'équilibre, Ph. D. thesis, Univerité de Nice (France), (1994).

[15] A. Michalke, On the inviscid instability of the hyperbolic-tangent velocity profile, J. Fluid Mech., vol. 19, (1965), pp. 543 - 556.

[16] P. L. Roe, Approximate Riemann Solvers, Parameter Vectors and Difference Schemes, J. Comp. Phys. 43, (1981), pp. 357-372.

[17] A. M. Rogerson and E. Meiburg, A Numerical Study of the Convergence Properties of ENO Schemes, J. Sci. Computing, Vol 5, no. 2, (1990).

[18] N. D. Sandham and W. Reynolds, The Compressible Mixing Layer: Linear Theory and Direct Simulation, AIAA J., vol. 28, (1989), pp. 618 - 624.

[19] N. D. Sandham, H. C. Yee, A Numerical Study of a Class of TVD Schemes for Compressible Mixing Layers, NASA Technical Memorandum, 102194 (1989).

[20] C.-W. Shu and S. Osher, Efficient Implementation of Essentially Non-oscillatory Shock-Capturing Schemes, J. Comp. Phys. 77, (1988), pp. 439 - 471.

[21] C.-W. Shu, Numerical Experiments on the Accuracy of ENO and MOdified ENO-schemes, J. Sci. Computing, vol 5, nb. 2, (1990).



Unité de recherche INRIA Sophia Antipolis
2004, route des Lucioles - B.P. 93 - 06902 Sophia Antipolis Cedex (France)

Unité de recherche INRIA Lorraine - Technopôle de Nancy-Brabois - Campus scientifique
615, rue du Jardin Botanique - B.P. 101 - 54602 Villers lès Nancy Cedex (France)
Unité de recherche INRIA Rennes - IRISA, Campus Universitaire de Beaulieu 35042 Rennes Cedex (France)
Unité de recherche INRIA Rhône-Alpes - 46, avenue Félix Viallet - 38031 Grenoble Cedex 1 (France)
Unité de recherche INRIA Rocquencourt - Domaine de Voluceau - Rocquencourt - B.P. 105 - 78153 Le Chesnay Cedex (France)

Éditeur
INRIA - Domaine de Voluceau - Rocquencourt - B.P. 105 - 78153 Le Chesnay Cedex (France)

ISSN 0249 - 6399

